The Pennsylvania State University

The Graduate School

Eberly College of Science

INSIGHTS INTO THE SYNTHETIC MECHANISMS BEHIND LIGAND-FREE METAL NANOPARTICLE FORMATION

A Thesis in

Chemistry

by

Rosemary M. Veghte

Submitted in Partial Fulfillment
of the Requirements
for the Degree of

Master of Science

May 2016

The thesis of Rosemary M. Veghte was reviewed and approved* by the following:

Thomas E. Mallouk
Evan Pugh University Professor of Chemistry,
Biochemistry and Molecular Biology, and Physics
Head of the Chemistry Department
Thesis Advisor

Raymond E. Schaak
DuPont Professor of Materials Chemistry

Benjamin J. Lear
Assistant Professor of Chemistry

*Signatures are on file in the Graduate School

ABSTRACT

The reactions catalyzed by metal nanoparticles are of great importance in a number of industries that range from synthesizing methanol to designing more efficient catalytic converters. An issue facing many of these processes comes in the form of nanoparticle sintering: coarsening and growth of metal nanoparticles caused by their need to lessen overall surface energy. The resulting nanoparticle growth that arises from this energetic need dramatically diminishes their catalytic activity. This, in turn, costs major industries time and money as they work to replenish the catalyst.

Past work has been done to more fully understand catalytic systems involving metal oxide/hydroxide nanoparticles deposited on a variety of early transition metal oxide supports. Through this work, it was found that an anomalous stabilization of the metal nanoparticles was possible when they were deposited on certain types of metal oxide supports. These studies were then expanded to include preliminary periodic trends that have been garnered from work done by high resolution transmission electron microscopy (TEM), isothermal titration calorimetry (ITC), and X-Ray diffraction (XRD). More recently, ligand-free, OH^- - stabilized Pt and Pd nanoparticles have been synthesized and characterized via the methods listed above. These ligand-free nanoparticles hold greater catalytic relevance because of their lack of bulky surface ligands, granting them with a higher available surface area for large-scale industrial reactions.

While the synthesis of these OH^- - stabilized ligand-free metal nanoparticles is of great importance, it is also necessary to understand their behavior in solution – how they form, how they remain dispersed, and so on – in order to formulate conditions that will preserve their stability. Presented here is work done to synthesize and characterize ligand-free Pt and Pd metal nanoparticles. Their reaction progress was monitored by UV-Visible spectroscopy, and intermediate reaction species will soon be determined by ^{195}Pt NMR. The final product was confirmed via TEM and XRD. The metal nanoparticles were then deposited onto sheets of calcium niobate ($KCa_2Nb_3O_{10}$), and the resulting reaction setup was exposed to temperatures up to 900°C to monitor their sintering under harsh conditions, with the overarching goal of understanding how metal nanoparticles interact with their support systems.

TABLE OF CONTENTS

LIST OF FIGURES

LIST OF ABBREVIATIONS

TWC	Three-Way Catalyst
NO_x	Nitrogen Oxide Compounds
SMSI	Strong Metal-Support Interactions
EMSI	Electronic Metal-Support Interactions
DFT	Density Functional Theory
XPS	X-Ray Photoelectron Spectroscopy
ITC	Isothermal Titration Calorimetry
TBA^+OH^-	Tetrabutylammonium Hydroxide
HR-TEM	High Resolution Transmission Electron Microscopy
TEM	Transmission Electron Microscopy
HSAB	Hard and Soft Acids and Bases Theory
STEM	Scanning Transmission Electron Microscopy
XRD	X-Ray Diffraction
UV-Vis	Ultraviolet-Visible Spectroscopy
NIR	Near Infrared Spectroscopy
NMR	Nuclear Magnetic Resonance Spectroscopy
EDS	Energy Dispersive X-Ray Spectroscopy
HAADF-STEM	High Angle Annular Dark Field Scanning Transmission Electron Microscopy
MCL	Materials Characterization Lab
NIST	National Institutes of Standards and Technology
DLS	Dynamic Light Scattering
ELS	Electrophoretic Light Scattering

ACKNOWLEDGEMENTS

First of all, I would like to thank my advisor, Dr. Tom Mallouk, for being a fantastic advisor. He was always patient and understanding with me, and he always made time for a lively discussion about science and/or life. I would also like to thank Dr. Ray Schaak and Dr. Ben Lear for serving on my committee. In addition, I would like to thank the members of the Mallouk group for their thoughts and ideas on various aspects of my research. They provided valuable guidance and lots of humor along the way.

I also want to thank my husband, Daniel, for always supporting me throughout my time here in graduate school. Whether it was listening to me complain or going off on a spontaneous adventure, Dan was always there to know exactly what to do. Without him, I would not be where I am today, and I am forever grateful.

Furthermore, I would like to thank my family for raising me to be forever curious of my surroundings. My mother always encouraged us to make new things, explore new places, and be forever observant of the tiniest details. Through her, I found joy in the sciences, and found my direction in the world. My father showed me that true happiness doesn't come in the form of money, and that I don't need to be at the top of my career field to be considered "successful." Success and happiness are what I make of them, and he showed me that working hard and still enjoying the smaller things in life lead to true happiness. Through him, I learned to work hard at what I do and always, always make time for fishing, a vegetable garden, and a good hike. Finally, I'd like to thank my little brother for making me the competitive person I am. I'm not sure I'd be here today if he wasn't always challenging me!

INSIGHTS INTO THE SYNTHETIC MECHANISMS BEHIND LIGAND-FREE METAL NANOPARTICLE FORMATION

CHAPTER 1:
INTRODUCTION

1.1 Nanoparticles in Catalytic Systems.

The bonding interactions at the metal/metal oxide interface are critically important for selecting catalysts in some of today's largest industrial settings.[1-4] For example, reactions involving supported copper nanoparticles have been widely used in methanol synthesis and organic compound hydrogenation.[4] Photochemical water splitting as a means of energy production has been investigated using transition metal nanoparticles as catalysts on early transition metal oxide supports.[2,5] However, transition metal nanoparticles in harsh catalytic conditions tend to undergo sintering, dramatically increasing their size and reducing their available surface area through mechanisms such as Ostwald ripening or coalescence. Ostwald ripening is a phenomenon that occurs when smaller nanoparticles in close proximity to larger ones seek to reduce their overall surface energy by merging with the larger nanoparticle. Coalescence is a product of nanoparticle migration initiated by Brownian motion, which causes smaller nanoparticles to combine with other smaller nanoparticles nearby to form larger, less mobile nanoparticles. In many industries, this leads to a premature loss in catalyst activity.

In the automotive industry, the catalysts in "three-way catalyst", or TWC, catalytic converters are often expected to work in unison with one another, oxidizing carbon monoxide and hydrocarbons while reducing various forms of nitrogen oxide compounds (NO_x).[6] More recently, the metal catalysts, such as Pt, Pd, and Rh, have begun to sinter more rapidly due to the catalytic converter's increasingly close placement to the engine.[6-9] This leads to decreased catalyst performance and lifetime. Encapsulation of a ceria-supported Pd automotive catalyst at 400°C has also been reported, with a gradual transition of Ce^{4+} to Ce^{3+} in the support.[7] With increasingly strict automobile emission guidelines, the metal catalysts used in modern catalytic converters must be designed to withstand higher temperatures (sometimes to 900°C) for longer periods of time.

The catalytic relevance of maintaining small particle size at the metal/metal oxide interface has been understood for decades, but successful methods for inhibiting nanoparticle growth have been limited. Numerous literature sources describe a loss of catalytic activity as metal nanoparticles such as platinum, palladium, rhodium, or gold

coarsen and migrate upon exposure to harsh catalytic conditions, such as temperatures exceeding 900°C or hydrogen gas.[1,10-12] Similar effects have been noted during a ZnO-supported Cu synthesis of methanol. While CuO is easily reduced to Cu metal, the issue lies in the behavior of the catalyst itself. Normally, a copper catalyst used in methanol manufacturing has a lifetime of several months.[4] Figure 1a details this process of nanoparticle ripening and migration as they encounter increasingly harsh environmental conditions. Initially, deposited nanoparticles are distributed with relative uniformity (per transmission electron microscope images). As increasingly harsh reaction conditions are applied (up to ~1000°C), nanoparticle coarsening and migration begin to occur in order to lower the overall surface energy of the nanoparticle. With coarsening comes a decrease in

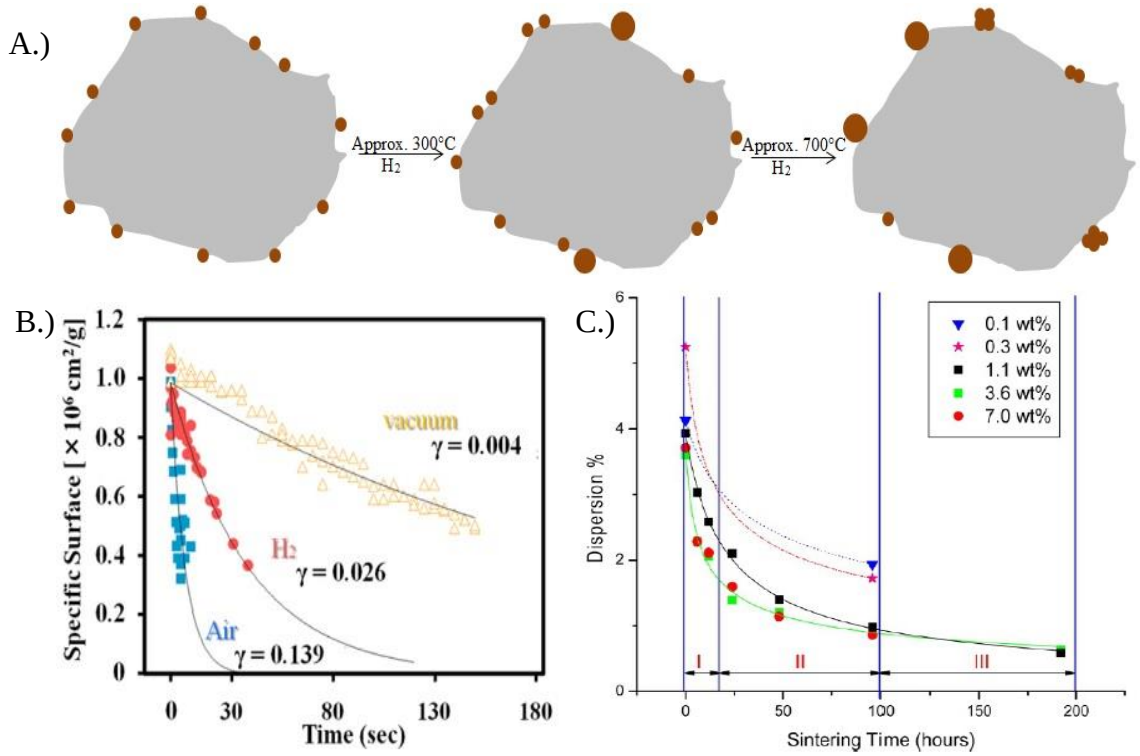

Figure 1. A.) Nanoparticle sintering occurring upon heating the metal oxide supports to temperatures exceeding 700°C. B.) Pt nanoparticles supported on carbon show a rapid loss of surface area when exposed to air, H_2, and vacuum TEM conditions.[13] C.) Pd nanoparticles deposited on alumina supports become less dispersed over time as they aggregate to lessen surface energy. These particular nanoparticles underwent treatment of 10% H_2O/N_2 at 900°C.[9]

nanoparticle surface area and thus a decrease in surface reactivity.[4] This is further proven in Figure 1b, which demonstrates the varying rates of catalyst decay when exposed to air, H_2, and vacuum conditions.[13] When exposed to air, the Pt on carbon catalyst experiences

the most severe reduction in surface area, signaling rapid coarsening and possibly aggregation of the Pt nanoparticles. This phenomenon is not uncommon; Figure 1c presents yet another example of nanoparticle aggregation and thus loss of surface area. Here, Pd nanoparticles deposited on an alumina support drastically decreased in % dispersion over the course of 100h. As nanoparticle sintering increased, the Pd nanoparticles became less dispersed and therefore less surface active.[9] While this may seem a long period of time in the lab, this time frame is a mere instant in major industries, where catalysts are expected to last for weeks, months, or years.

1.2 Strong Metal-Support Interactions.

It was originally theorized by Tauster and Fung that a strong metal-support interaction (SMSI) was the main inhibitor to nanoparticle growth, as it involved encapsulation of the nanoparticles by the metal oxide support.[14] Through spectroscopic methods, it was determined that this process was initiated by an electron transfer from a cation in the metal oxide support to the surface of the metal nanoparticle.[14] This SMSI model held true for numerous metal nanoparticle/metal oxide support systems: chemisorption of H_2 and CO_2 in systems comprised of Pt/TiO_2, Rh/TiO_2, Pd/TiO_2, etc. was markedly lower when heated in vacuum to temperatures exceeding 500°C.[15] The strong metal support interactions are amplified further upon n-type doping of a low-surface energy metal oxide support.[16] Metals such as Pt, Pd, Rh, and Ir, with their large work functions, also promote encapsulation by the oxide support upon heating to temperatures necessary for nanoparticle migration.[16] In an effort to reduce the effects caused by SMSI and increase catalyst activity, studies of the electronic structure of bonding were conducted to further understand the bonding interface.[17]

Eventually, the SMSI theory began to break down in systems where a late transition metal nanoparticle was deposited on a ZnO support.[18] Liu et al. reported changes in electron transfer that were dependent upon the environmental conditions surrounding the metal nanoparticle/metal oxide support system (see Figure 2).[18] When exposed to the traditional highly reducing conditions found in catalytic processes, the Au nanoparticles involved in the study were reduced and became incorporated in the ZnO support structure to form a conductive AuZn alloy. Exposing the system to highly oxidative conditions

reverses the process, reducing the metal oxide support and encouraging Au nanoparticle encapsulation by the ZnO support. Encapsulation of the Au nanoparticle by the support occurred under strongly oxidative conditions (300°C under O_2) rather than the traditional reducing conditions that were supported by SMSI.[18]

Several methods to physically segregate nanoparticles were employed in order to prevent nanoparticle migration and sintering. For instance, Au nanoparticle growth on porous alumina supports was greatly reduced due to physically restraining the nanoparticles.[19] The 2nm Au nanoparticles were dispersed on porous, ~15nm-thick alumina supports and heated to temperatures exceeding 700°C. Upon calcination at these temperatures and above (to 900°C), Wang et al. observed no significant increase in size of the Au nanoparticles. They retained their original shape and size due to containment in the porous alumina, which also restricted any appreciable nanoparticle migration.[19] The prominence of electronic metal-support interactions (EMSI), seen below, has also been investigated by essentially encapsulating TiO_2- or CeO_2- supported Pt nanoparticles in porous SiO_2 to energetically prevent Pt nanoparticle migration. Because of the weak interactions between SiO_2 and the metal oxide support, the SiO_2 does not interfere with the strong bonding between the metal nanoparticle and support; it simply prevents migration and nanoparticle growth at temperatures up to 750°C and preserves catalytic activity.[20]

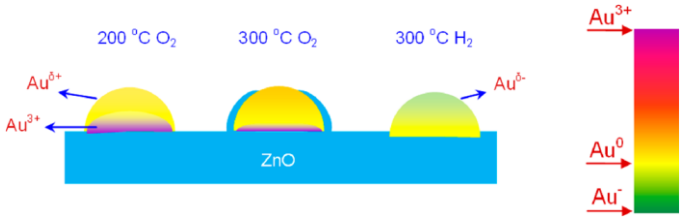

Figure 2. Here, gold nanoparticles are deposited onto a ZnO support and exposed to varying oxidizing and reducing environmental conditions, as well as temperature fluctuations.[18]

1.3 Electronic Metal-Support Interactions.

More recently, electronic metal-support interactions (EMSI) between metal nanoparticles and their metal oxide supports have been used to explain the strong bonding observed between certain metals and their supports.[21,22] Rodriguez et al. have observed more pronounced EMSI when the catalyst support is embedded with small, 2-4nm metal nanoparticles.[22] Many reports suggest that ceria supports promote electronic interactions

between themselves and the metal (Au, Ag, Pt, etc.), thus lowering the risk of nanoparticle sintering.[23-25] Density functional theory (DFT) calculations also suggest a 20-50kJ/mol increase in bonding energy between metal nanoparticles and their supports when the support is composed of ceria.[23] No nanoparticle migration or sintering was observed when Ag was deposited onto ceria supports, and isothermal titration calorimetry data suggested very strong bonding interactions.[23]

These strong bonding interactions (and their subsequent ability to reduce metal nanoparticle sintering) have generated appreciable interest in recent years. The fundamental chemistry behind it has been attributed to SMSI and EMSI, but recent work has suggested that the bonding interactions may be more complicated.[26,27] Bonding between the *d*-electrons of the metal and metal oxide is often shared covalently rather than by electron transfer pathways.[26,28] In other words, it was possible to formulate a metal/metal oxide catalyst system that did not rely on physically segregating the nanoparticles. Nanoparticle encapsulation by the support through SMSI was also greatly reduced due to these strong bonding interactions; in fact, with certain combinations of late transition metal nanoparticle and metal oxide supports, nanoparticle sintering and growth were not observed.[27]

With new insights into the behavior of metal nanoparticle bonding to their early transition metal oxide support, recent work by Hata et al. serendipitously demonstrated the catalytic prowess of $\leq$ 5nm reduced $Rh(OH)_3$ nanoparticles deposited on exfoliated $KCa_2Nb_3O_{10}$ and later $K_4Nb_6O_{17}$.[2,29] While exploring the degree of encapsulation of various metal nanoparticles, it was found that an anomalous stabilization of rhodium oxide and hydroxide nanoparticles was observed when they were evenly dispersed on niobate supports.[2] In this same study, it was found by X-ray photoelectron spectroscopy (XPS) that the Rh metal was covalently bound to the Nb of the support through an oxygen bond. Further measurements concluded that the rhodium oxide/hydroxide stabilization was caused by interfacial bonding interactions. While this was noted, calorimetric investigations into the actual strength of these bonds were not launched until several years later.[27,30,31]

1.4 Calorimetric Measurements of Strong Bonding.

Calorimetric measurements of bonding enthalpy are often conducted through isothermal titration calorimetry (ITC), which was originally designed to measure heat of bonding changes in biopolymers.[32] The ITC itself, shown here in Figure 3, is comprised of a two-cell system enclosed in a thermal jacket. The sample, in this case metal nanoparticles (or their precursor) are injected into the sample cell, which contains the exfoliated metal oxide supports (typically $KCa_2Nb_3O_{10}$, in the exfoliated form of $TBA_{0.24}H_{0.76}Ca_2Nb_3O_{10}$). The heat produced in the exothermic reaction disrupts the isothermal nature of the cells. Power is then supplied to the reference cell, which contains the pure solvent (the same solvent as that used in the sample cell), until both cells are once again at an equilibrium. This sharp increase in power is then monitored as a function of injection number. Integration of the peaks produces a sigmoidal curve by which the total range of ΔH during the reaction can be observed.

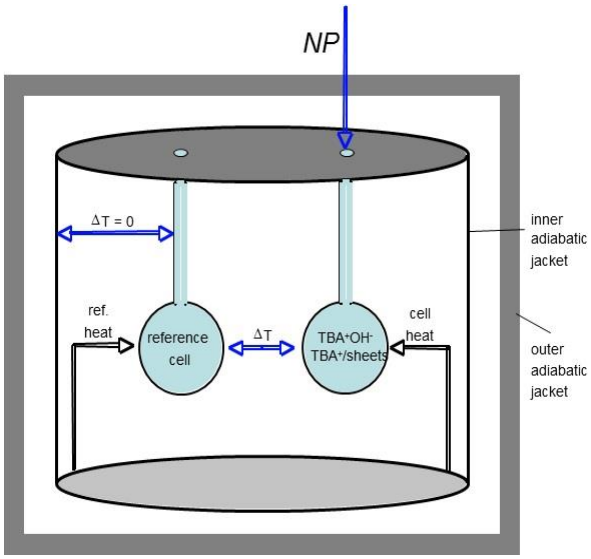

Figure 3. A schematic of a typical isothermal titration calorimeter (ITC). The sample is injected into the sample cell, and the power supplied to the reference cell to maintain isothermal conditions is measured.[27]

The Campbell group, among others, has been at the forefront of calorimetry research for several years now. Many of their molecular interactions of focus are centered around a metal nanoparticle's performance as a catalyst in various high-throughput industrial reactions that include methanol reformation, catalytic converter sanitation, and organic molecule oxidation.[30,33-35] Their calorimetric work has quantified the stability of an adsorbed H_2O/OH^- layer on Pt(111) nanoparticles, a required intermediate step in many

industrial reformation processes.[34] Experiments stemming from this work may even be able to characterize the hydrogen bond strengths within the adsorbed H_2O/OH^- layer on the surface of metal nanoparticles, providing information on the fundamental chemistry behind these interactions. Additionally, they have demonstrated that the type of metal oxide support strongly influences the probability that small, <6nm catalytic nanoparticles will sinter upon exposure to strongly reducing conditions. For example, Ag nanoparticles were deposited onto CeO_2, Fe_3O_4, and MgO supports, and their resulting bonding enthalpy was measured via calorimetry. It was found that Ag nanoparticles deposited onto CeO_2 supports were more stable than those deposited onto MgO and exhibited far slower coarsening.[23,36] Similarly, Au nanoparticles in this same regime maintained their catalytic activity in the 3nm-5nm range, but activity was significantly diminished after they had sintered and grown to ≥6nm (Campbell). Without this pioneering work, much would still be unknown about the mechanics behind metal nanoparticle sintering on metal oxide supports.

Recent work in the Mallouk group has utilized ITC in a similar manner: parting ways with its traditional biological uses, isothermal titration calorimetry was used to directly measure the total heat of bonding that occurred when a $Rh(OH)_3$ solution of mass fraction 0.01 was injected onto exfoliated $TBA_{0.24}H_{0.76}Ca_2Nb_3O_{10}$ nanosheets.[27] Per the Born-Haber cycle, the actual enthalpy of bonding between the $Rh(OH)_3$ nanoparticles and the $KCa_2Nb_3O_{10}$ was discerned from the total enthalpy of the reaction, including those of the acids and bases:

$$RhCl_2(OH)(H_2O)_{3(aq)} + 2TBA^+OH^-_{(aq)} \rightarrow Rh(OH)_{3(s)} + 2TBA^+Cl^- + xH_2O_{(l)} \qquad \Delta H_1$$

$$HCl_{(aq)} + TBA^+OH^-_{(aq)} \rightarrow TBA^+Cl^-_{(aq)} + H_2O_{(l)} \qquad \Delta H_2$$

$$Rh(OH)_{3(s)} + TBA^+ / sheets^-_{(s)} \rightarrow Rh(OH)_3/sheets^-_{(s)} + TBA^+_{(aq)} \qquad \Delta H_3$$

$$RhCl_2(OH)(H_2O)_{3(aq)} + 3TBA^+OH^-_{(aq)} + HCl_{(aq)} + TBA^+ / sheets^-_{(s)} \rightarrow Rh(OH)_3/sheets^-_{(s)} + 3TBA^+Cl^-_{(aq)} + xH_2O_{(l)} \qquad \Delta H_4$$

Shown here, ΔH_1 is the enthalpy of hydrolysis of the aqueous $RhCl_3$ precursor. ΔH_2 is a measurement of heat produced by the neutralization of a strong acid and strong base. The enthalpy measurement of interest, the enthalpy of bonding between the metal nanoparticles and their metal oxide support, is listed here as ΔH_3. It is calculated by:

$$\Delta H_3 = \Delta H_4 - \Delta H_2 - \Delta H_1,$$

where the bonding enthalpy between the metal and the support, ΔH_3, can be determined by subtracting the values of ΔH_1 and ΔH_2 from the overall reaction enthalpy, ΔH_4. These values are all known and are previously measured. ΔH_2, the enthalpy of HCl and TBA^+OH^- neutralization, is measured directly by titrating HCl with TBA^+OH^-. The enthalpy of hydrolysis of the aqueous $RhCl_3$ precursor is calculated after measuring the total heat released when $RhCl_3(H_2O)_3$ was injected into a TBA^+OH^- solution in the ITC. This produces a value equivalent to $\Delta H_1 + \Delta H_2$. Because ΔH_2 is a previously measured value, ΔH_1 is calculated using these known values.[27] The enthalpy value of interest, ΔH_3, is then easily calculated.

ITC results have revealed much about the bonding behavior of metal oxide and hydroxide nanoparticles to metal oxide supports. Through this calorimetric method, it was found that exothermic bonding interactions between metal nanoparticles and their metal oxide supports prevents nanoparticle coarsening by promoting a favorable interaction between the nanoparticle and the support.[27] The stronger the bonding between these two materials, the greater the likelihood that the nanoparticles would remain tightly bound to their support, reducing migration and ultimately coarsening and the loss of catalytic activity.[27] This trend is observed quantitatively by comparing ITC data for $Rh(OH)_3$ nanoparticles deposited on a variety of supports ranging from TBA^+OH^- - exfoliated $KCa_2Nb_3O_{10}$ ($TBA_{0.24}H_{0.76}Ca_2Nb_3O_{10}$) to SiO_2 and γ-Al_2O_3. Interestingly, the heat of bonding of the $Rh(OH)_3$ nanoparticles to SiO_2 and γ-Al_2O_3 is positive, meaning the heat of bonding to the support is endothermic, while the opposite holds true for the metal hydroxide nanoparticles on metal oxide supports. $Rh(OH)_3$ on $TBA_{0.24}H_{0.76}Ca_2Nb_3O_{10}$ produced an exothermic heat of bonding and in return had minimal coarsening and migration.[27]

1.5 High Resolution Transmission Electron Microscopy for Metal Nanoparticle Observations.

Further insights into the sintering and growth of metal nanoparticles on transition metal oxide supports can be gained through the use of *in-situ* high resolution transmission electron microscopy (HR-TEM). By using the preparation method detailed in Figure 4, the response of ~1nm-thick nanosheets containing deposited metal nanoparticles in temperatures up to 900°C and under H_2 reducing conditions can be monitored. Here, Dion-Jacobsen perovskite supports (commonly $KCa_2Nb_3O_{10}$ or $K_4Nb_6O_{17}$) are synthesized via solid state methods.[2, 37]

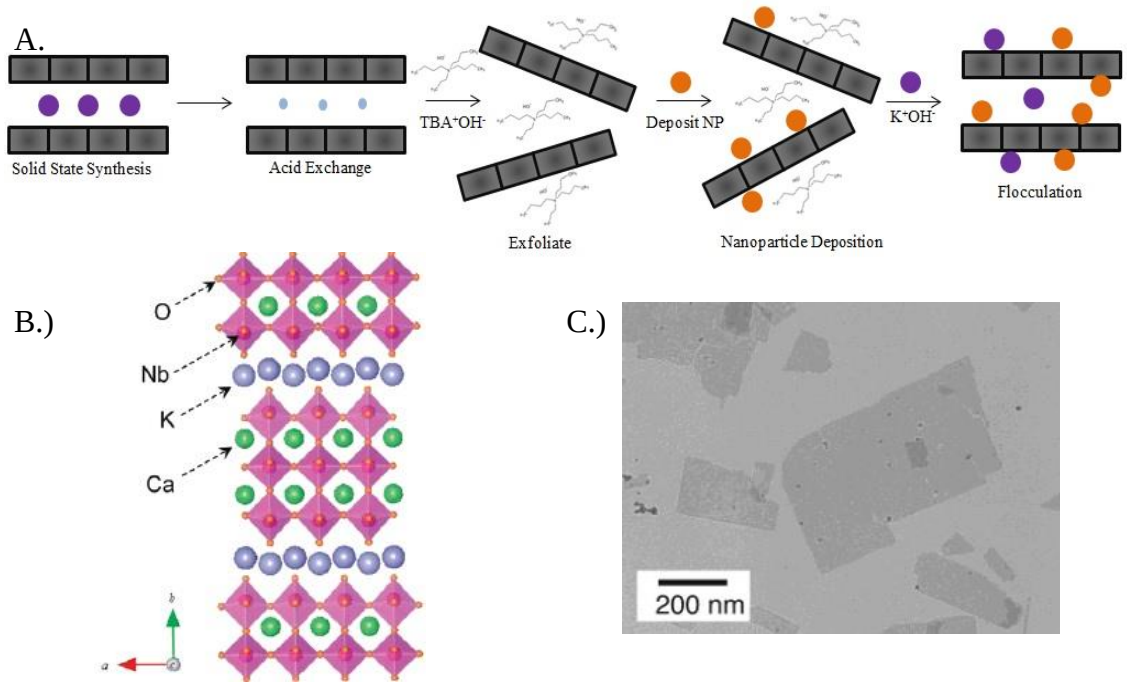

Figure 4. A.) Solid state synthesis of transition metal oxide nanosheets followed by acid exchange and subsequent exfoliation. Metal nanoparticles are then deposited onto these sheets, and they are restacked for observation by TEM. B.) Layered structure of a Dion-Jacobsen $KCa_2Nb_3O_{10}$ support.[38] C.) Platinum nanoparticles deposited on $KCa_2Nb_3O_{10}$ supports. Supports are typically 1nm in thickness and 200nm-300nm in length.[39]

Following synthesis, the bulk $KCa_2Nb_3O_{10}$ is proton-exchanged using nitric acid. Proton exchange is a necessary step in the exfoliation process, as the newly-added H^+ cations facilitate the intercalation of the large, basic TBA^+OH^- molecule. Proton exchange is then followed by exfoliation with the TBA^+OH^- molecule, whose bulky side groups aid in separating the bulk $KCa_2Nb_3O_{10}$ into ~1nm-thick sheets. Following periodic acid-base

trends, Group 6 cations are more easily exfoliated than those found in Group 4 or 5 due to their stronger acidic nature.[40] Nanoparticles are then deposited onto the exfoliated sheets and restacked using K^+, Na^+, or H^+ cations. The restacked sheets, while less uniform, are thin enough for HR-TEM observation of sintering in highly reducing environmental conditions.

Work from the Mallouk group regarding the behavior of metal hydroxide nanoparticles as possible catalysts had produced several interesting results. Considering the growth of $Rh(OH)_3$ nanoparticles when deposited on $KCa_2Nb_3O_{10}$, the nanoparticles actually underwent reverse Ostwald ripening when simply loaded into TEM.[27] This behavior was observed without exposure to excessive heating or reducing environmental conditions and produced well dispersed $Rh(OH)_3$ nanoparticles under 1nm in size. Furthermore, as can be seen in Figure 5a and b, the Rh_2O_3 nanoparticles retained their small diameter when heated to temperatures upwards of 700°C. Beginning at 200°C and heating up to 700°C, the Rh_2O_3 nanoparticles coarsened slightly, from 1nm to approximately 5nm on the $KCa_2Nb_3O_{10}$ support. Compared to other catalysts, which coarsen at significantly higher amounts, this small change of several nanometers demonstrates a promising new metal nanoparticle/metal oxide support system that could perform much more efficiently as a catalyst/support system.[27,41-43]

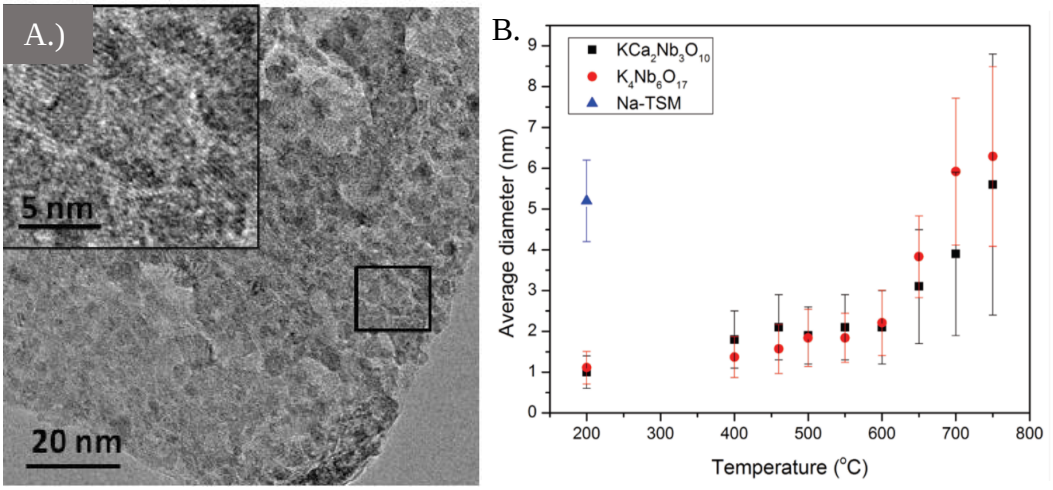

Figure 5. A.) presents the absence of Rh_2O_3 nanoparticle coarsening at temperatures exceeding 500°C; they maintain their approximate size of 1-2nm. B.) corroborates this finding, as the Rh_2O_3 nanoparticles increase in size from approximately 1nm to approximately 5nm, a small change given the harsh environmental conditions to which the nanoparticles are exposed.[27]

1.6 Ligand-free Metal Nanoparticles.

Investigating the bonding that occurs between a metal nanoparticle and a metal oxide support has been expanded recently to include ligand-free metal nanoparticles, which are shown to be among the most surface active materials in catalytic reactions.[44] These nanoparticles (of the Au, Pt, and Pd variety) are often <5nm in diameter and present very exciting opportunities for further understanding nanoparticle coarsening under harsh catalytic conditions. Ligand-free metal nanoparticles are of greater catalytic relevance than their metal oxide nanoparticle predecessors because they lack the bulky surface ligands that reduce contact between the metal nanoparticle and their supporting material. Shown below in Figure 6 is the basic overview of the synthetic steps taken to produce ligand-free metal nanoparticles. Here, a metal halide precursor is hydrolyzed in base to produce a variation of a $M(OH)_n(H_2O)_y^{x-}$ species. As H^+ is introduced as a product of hydrolysis of a metal halide, the overall reaction pH is lowered, forming neutral $M(OH)_n$ species, which are stabilized in solution by the remaining $M(OH)_n(H_2O)_y^{x-}$. The $M(OH)_n$ nanoparticles can be further reduced by addition of methanol, which yields OH^- -stabilized metallic nanoparticles. The excess of OH^- in the solution is likely adsorbed to the nanoparticle surface, which separates the <5nm particles from one another. Hence the term "ligand-free metal nanoparticles."

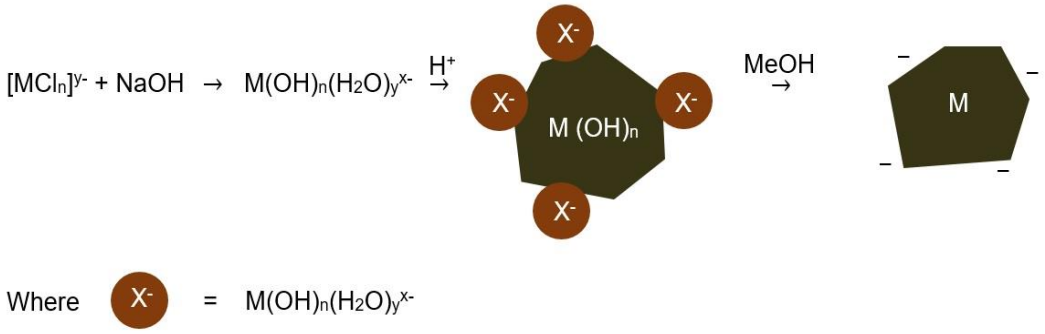

Figure 6. The synthetic steps of a ligand-free metal nanoparticle synthesis.

Ligand-free metal nanoparticles have been synthesized using various laser ablation techniques, but their stability in solution has long remained a mystery.[45,46] In accordance with Pearson's Hard and Soft Acids and Bases (HSAB) theory, ligand-free metal nanoparticles with similar polarizability to their surrounding environment will experience stronger binding interactions than nanoparticles whose surface polarizability differs strongly from that of their surroundings.[47] This means that a negative surface charge on the

ligand-free Pt and Pd nanoparticles is necessary for stabilization in a solution surrounded by OH^-. The negative charge is then transferred from the anion to the nanoparticle surface, which results in greater electrostatic stability. Interestingly, in ligand-free gold and silver nanoparticle systems synthesized by laser ablation, the concentration of anions in solution directly affected the coalescence and growth of the nanoparticles. Lower concentrations of dissolved ions in solution have been shown to prevent growth in ligand-free metal nanoparticles through direct interactions with the nanoparticle surface.[48-50] It appears that mM to μM concentrations of dissolved ions provide sufficient surface stabilization to the ligand-free metal nanoparticles, resulting in a smaller size distribution and a smaller likelihood for significant growth. However, in these systems, a change in the salinity of the system can have drastic consequences for the stability of the nanoparticle system in solution. In this case, an elevated concentration of NaOH in solution can lead to immediate aggregation of the ligand-free Pt nanoparticles, indicating a loss of stability in solution.

Methods for synthesizing a multitude of ligand-free metal nanoparticles, including Pt, Pd, Au, and Ir, are currently underway. Current efforts are focused towards synthesizing stable ligand-free Pt and Pd nanoparticles with the expectation that this list will increase in length. Each synthesis is strongly affected by changes in concentration and reaction pH, so efforts are being made to find the exact measurements needed for stable nanoparticles. Heated high resolution TEM/STEM efforts will provide further insights into the ligand-free nanoparticles' behavior when exposed to high temperatures and strongly reducing H_2 conditions. The surface behavior of the ligand-free metal nanoparticles is being investigated via zeta potential measurements. These measurements seek to provide valuable information regarding the surface charges of the collective nanoparticle solution while also providing further insight into their stability and shelf life. Future studies will use isothermal titration calorimetry to understand the strong bonding structure of the ligand-free metal nanoparticles and various transition metal oxide supports. Current efforts are currently being taken to vary the type of nanoparticle on $KCa_2Nb_3O_{10}$ supports, with the goal of expanding these results to include various types of late transition metal nanoparticle on early transition metal oxide supports. With this information, valuable periodic trends regarding the fundamental chemistry behind the choice of a catalyst/support system can be identified and utilized.

CHAPTER 2:
MATERIALS AND METHODS

2.1. Synthesis of Ligand-free Metal Nanoparticles and Transition Metal Oxide Supports.

The ligand-free metal nanoparticles were prepared by hydrolyzing a 0.01 mmol solution of a metal halide precursor material in a 100mL 3-neck flask from its original K_2MCl_6 (or K_2MCl_4) state to a $M(OH)_n(H_2O)_y^{x-}$ species using 35mL of a 0.05M NaOH (EMD, ACS Grade) solution prepared in a 100mL volumetric flask. Here, the platinum precursor was in the form of K_2PtCl_6 (99.99%, Sigma Aldrich) while the palladium precursor was K_2PdCl_4 (98%, Sigma Aldrich). Ideally, the NaOH solution must have a pH of approximately 12. The pH of the NaOH solutions used here varied between 12.2-12.4 depending on the batch, as measured by a VWR sympHony SP70P pH meter. The $M(OH)_n$ intermediate species were then reduced with 15mL EMD Millipore DriSolv® methanol to their elemental state and stabilized by the remaining OH^- in solution; these species are never bound to the metal nanoparticle. Refluxing at 85°C for 4-6 hours, the Pt nanoparticle solution changed from clear to light yellow to brown; the reaction was at completion when a murky, dark brown color emerged.[51] This synthetic method produced a 0.2mM Pt nanoparticle solution. The success of the reaction was highly dependent upon the pH: reactions performed at an initial pH < 12 or pH > 13 were not hydrolyzed. It was found that an initial pH range of 12.2-12.4 was ideal. The pH of a typical synthesis was monitored via pH meter: when 0.05M NaOH and methanol were added to the K_2PtCl_6 precursor, the pH was 12.3. When the first color change was seen, from clear to light yellow, the reaction pH fell to 11.6. Throughout the course of the reaction, the pH remained relatively stable at 11.6, even though the reaction changed from clear to light yellow to dark brown. This small decrease in pH is perhaps caused by the incorporation of OH^- anions into $M(OH)_n(H_2O)_y^{x-}$ and the subsequent release of H^+ and Cl^- into the solution. Attempts were made to scale up the reaction by twofold and threefold, although these attempts were rendered unsuccessful when a color change failed to occur, even after 72 hours of reflux.

When the reaction pH was 13 or higher, a viscous material that completely encapsulated the nanoparticles formed. Figure 7, shown below, outlines the stark differences in product composition when the reaction pH is changed from between 12.2 –

12.4 to greater than 13. At left is the product of a ligand-free Pt nanoparticle synthesis done at pH = 13. When compared to the product of the same reaction done at pH = 12.4, it can be seen that the sample on the left has the majority of what is presumed to be Pt nanoparticles engulfed in a viscous fluid. This viscous material may consist of the hydrolyzed metal halide precursor and the anionic $M(OH)_n(H_2O)_y^{x-}$, which is formed as a result of hydrolysis of the precursor material, in an intermediate phase. The nanoparticles are not yet stabilized in adsorbed hydroxide anions; they are seemingly suspended in a basic, $M(OH)_n(H_2O)_y^{x-}$ coordination. Considering the small pH window in which nanoparticle stability is ensured, it is entirely possible that adjusting the solution pH interrupted the balance between $M\text{-}O^-$, M-OH, and $M\text{-}OH_2^+$, resulting in an agglomeration.

The support, calcium niobate ($KCa_2Nb_3O_{10}$), was synthesized using a modified procedure from Ebina et al. Here, stoichiometric quantities of Nb_2O_5, $CaCO_3$, and K_2CO_3

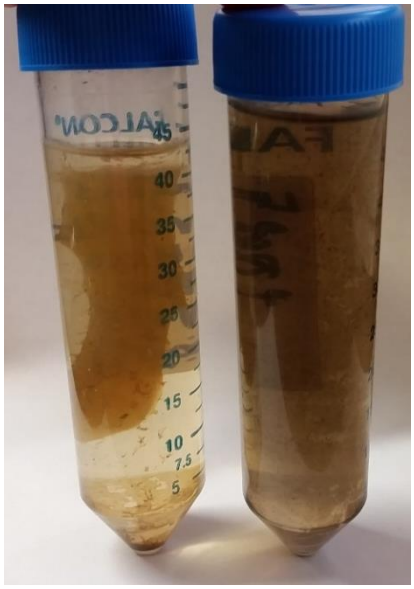

Figure 7. Examples of how minor adjustments in pH can affect the viscosity of the product. Shown at the left is a product of the ligand-free Pt synthesis done at pH > 13. At the right is the product of the same reaction; however the reaction pH was <13.

(40% excess) were mixed and heated to 1200°C for 12h.[39] An excess of K_2CO_3 was included to maintain the proper ratio of potassium after accounting for its evaporative loss during the synthesis. To deposit the ligand-free metal nanoparticles onto the $KCa_2Nb_3O_{10}$ supports, solutions of varying wt. % of Pt (1-5 wt. %) were added to 50mL of the exfoliated $KCa_2Nb_3O_{10}$ and shaken gently for 18 hours at room temperature. This is an adequate time frame to allow for nanoparticle deposition followed by re-stacking of the $KCa_2Nb_3O_{10}$

sheets by KOH. The resulting solution was then washed in triplicate, centrifuged down, and dried in a 60°C oven for 48 hours. Re-stacking of the Pt-bearing $TBA_{0.24}H_{0.76}Ca_2Nb_3O_{10}$ sheets allows for optimal viewing by transmission electron microscopy (TEM). Various other metal oxide supports have been synthesized, as can be seen in the following sections.

2.2. Synthesis and Characterization of Titanate Metal Oxide Supports

Attempts were made to synthesize quantities of $Cs_xTi_{2-(x/4)}\square_{(x/4)}O_4$, $(Cs_2O)_{0.3}Ti_2O_4$, Cs_2TiO_3, and $Cs_2Ti_5O_{11}$ using modified synthetic procedures.[52-55] Stoichiometric quantities of anatase TiO_2 and Cs_2CO_3 were combined in varying quantities to achieve these ratios. Additionally, the $Cs_xTi_{2-(x/4)}\square_{(x/4)}O_4$ synthesis required a de-carbonation step consisting of 1h of baking at 800°C before being heated to 800°C for 20h. It was suggested to remove the sample after 20h, re-grind, and place it back into the oven at 800°C for 20h to produce a phase pure $Cs_xTi_{2-(x/4)}\square_{(x/4)}O_4$ sample, but it was found that by doing this, additional phases were introduced into the material.[53] $(Cs_2O)_{0.3}Ti_2O_4$ was also synthesized via solid state methods, where varying molar ratios of TiO_2 to $CsNO_3$ (from 2.6 – 3.2) were used to create a single molten crystal of product.[54] This result was obtained when Ti:Cs was <3.0 and the reaction temperature was >1115°C. The most promising support, an easily-exfoliated $Cs_2Ti_5O_{11}$, was synthesized using 1:4.5 molar ratio of Cs_2CO_3 to TiO_2 rather than 1:5 molar ratio to account for evaporative loss of cesium during the synthesis.[52] This was done at 1000°C for 20h. Phase purity of these compounds was determined using powder x-ray diffraction on a PANalytical XPert Pro MPD system with a Cu Kα of 0.154 nm.

Much effort was put forth into synthesizing phase pure cesium titanate ($Cs_2Ti_5O_{11}$) supports, with limited success originating from the use of a preparative technique introduced by Sasaki et al.[52] A pentatitanate perovskite was chosen as a possible support material due to its inherently acidic nature, which would promote proton exchange and subsequent exfoliation. These pentatitanates also contain near-cubic interlayer galleries that allow for K^+ and Cs^+ cation intercalation.[52] Solid state synthesis of these $Cs_2Ti_5O_{11}$ supports per:

$$Cs_2CO_3 + 5TiO_2 \rightarrow Cs_2Ti_5O_{11} + CO_2$$

yielded the product of highest phase purity when the molar ratio of Cs_2CO_3 to TiO_2 was 1:4.5, which took into account the evaporative loss of cesium during synthesis. Shown below in Figure 8 is a time-based X-ray diffraction (XRD) comparison of $Cs_2Ti_5O_{11}$ when synthesized over periods of 24 and 48 hours, respectively. Percent composition was determined using the MDI Jade software. Synthesis using the advised 20h-24h yielded $Cs_2Ti_4O_9$ with a >50% TiO_2 contamination at 2θ values of 26°, 31°, and 34°. Both rutile and anatase TiO_2 phases were found: rutile TiO_2 was observed at 2θ = 26°, while the 2θ values at >30° were primarily anatase. Doubling the time of synthesis from 24h to 48h with the hope of consuming additional TiO_2 did not significantly aid in removing the TiO_2 contamination from the product; it was still primarily $Cs_2Ti_4O_9$ with >50% TiO_2 contamination. While the contents were stored at room temperature in a desiccator, it is of note to mention that the $Cs_2Ti_5O_{11}$ perovskite maintains a structure of $Cs_2Ti_5O_{11}\cdot(1+x)H_2O$ at temperatures below 200°C.[55]

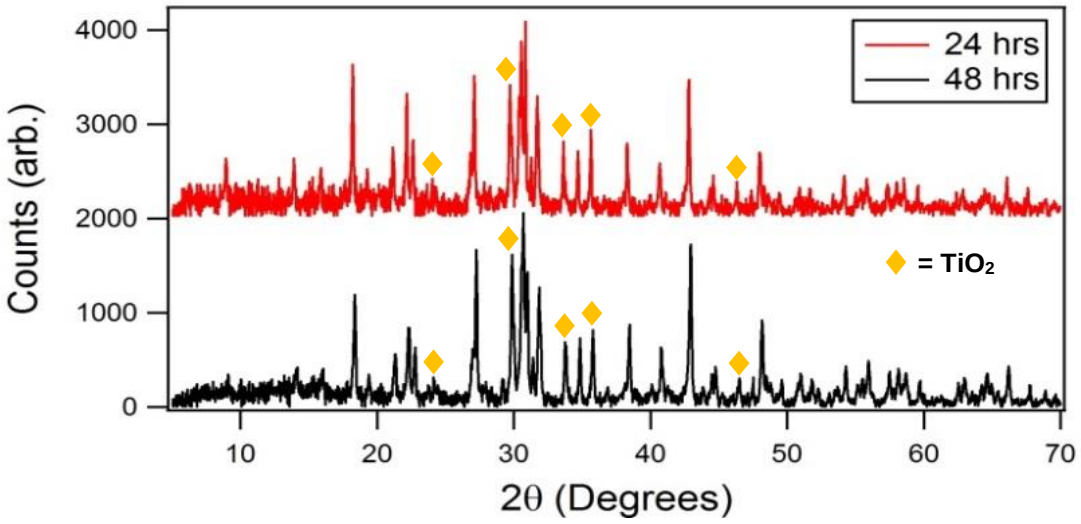

Figure 8. X-ray diffraction (XRD) patterns of products from a 24h and a 48h synthesis of $Cs_2Ti_5O_{11}$.

2.3. Synthesis and Characterization of the Vanadate Supports $K_3V_5O_{14}$ and KV_3O_8

To understand the periodic bonding trends of metal nanoparticles on early transition metal oxide supports, various forms of vanadate supports were synthesized as well. The most success in terms of phase pure products came in the form of $K_3V_5O_{14}$ and KV_3O_8, whose synthesis was adapted from the method designed by Kudo et al.[56] $K_3V_5O_{14}$ was synthesized using:

$$3K_2CO_3 + 5V_2O_5 \rightarrow 2K_3V_5O_{14} + 3CO_2$$

at 446°C for 5 hours. The resulting product was a dark red/orange powder with several unidentified black spots. Analysis using MDI Jade revealed that the product (shown in Figure 9, bottom) was 85.1% the desired material, $K_3V_5O_{14}$, and 14.9% KVO_3. The characteristic KVO_3 peak was found at a 2θ of 29°; however, KVO_3 is normally white to

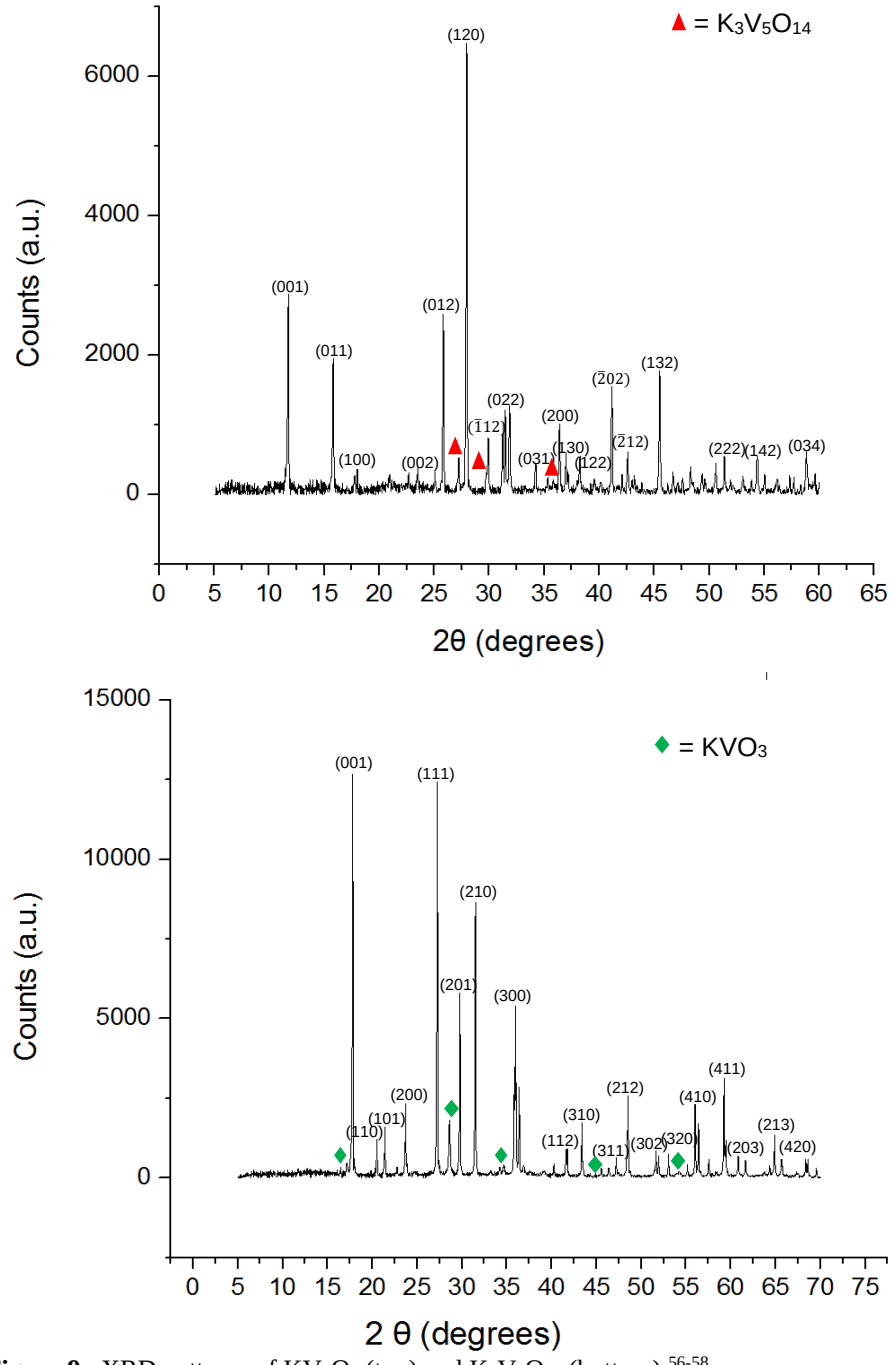

Figure 9. XRD patterns of KV_3O_8 (top) and $K_3V_5O_{14}$ (bottom).[56-58]

light yellow in color, so it was not the source of the black material found in the $K_3V_5O_{14}$ product. Per the formula below, KV_3O_8 was synthesized with limited success via:

$$K_2CO_3 + 3V_2O_5 \rightarrow 2KV_3O_8 + CO_2$$

at 457°C for 10h. Figure 9 (top) is a characteristic x-ray diffraction (XRD) pattern of the normal result of this reaction. It was found using Jade that the KV_3O_8 product was approximately 91.6% pure, with an 8.4% contamination by $K_3V_5O_{14}$. Diffraction patterns of various samples of K_2CO_3 revealed that some brands of K_2CO_3 are not consistently pure, which likely affected the outcome of the vanadate syntheses. Further work with vanadate compounds revealed much difficulty with exfoliating them. Exfoliation of the bulk layered materials was necessary for intercalating metal nanoparticles, as they will not permeate into the interlayer galleries of a bulk metal oxide material. Examination of a vanadate Pourbaix diagram also indicated decreased solubility of select vanadate compounds in water at pH values of >10.[59] Considering that exfoliation with the bulky TBA^+OH^- occurs under basic conditions, it was found that complete exfoliation of vanadate compounds could not be accomplished.

2.4. Characterization of Ligand-Free Platinum Nanoparticles by UV-Visible Spectroscopy, X-Ray Diffraction, and Transmission Electron Microscopy

UV-Visible (UV-Vis) spectroscopy was used to effectively monitor the reaction progress of K_2PtCl_6 with 15mL DriSolv® methanol and 35mL of 0.05M NaOH for 5 hours. Shown below in Figure 10 are UV-Vis spectra taken with a Varian Cary 6000i UV-Vis-NIR Spectrophotometer over a period of several hours. Figure 10a, the UV-Vis spectrum of the aqueous K_2PtCl_6 precursor and the final Pt nanoparticle solution, shows a strong absorbance at a wavelength of 260nm. This corresponds to a $PtCl_6^{2-}$ species, which would be present in solution after the precursor is dissolved in water, but before reduction from Pt(IV) to Pt(0).[51,60] In Figure 10c, a rapid loss of the 260nm peak is seen upon addition of methanol to the reaction solution containing 0.01 mmol K_2PtCl_6 and 35mL 0.05M NaOH, with the peak completely disappearing in under 5 minutes. Almost simultaneously, however, a shoulder appears at λ = 210nm, and a new peak develops at a wavelength between 300nm – 325nm. These peaks increase in size as the reaction time continues to 5 hours. The growth of these peaks as the $PtCl_6^{2-}$ peak disappears is an indication of the

evolution of new Pt species in solution, although UV-Vis cannot clearly illustrate these differences. The growth of the peak at a wavelength of 300nm – 325nm may perhaps be an indicator of the formation of the hydrolyzed product, $H_2Pt(OH)_6$.[61] As the reaction progresses, a greater concentration of the possible $H_2Pt(OH)_6$ product is formed; however, it remains a part of the solution even as the reaction reaches completion.

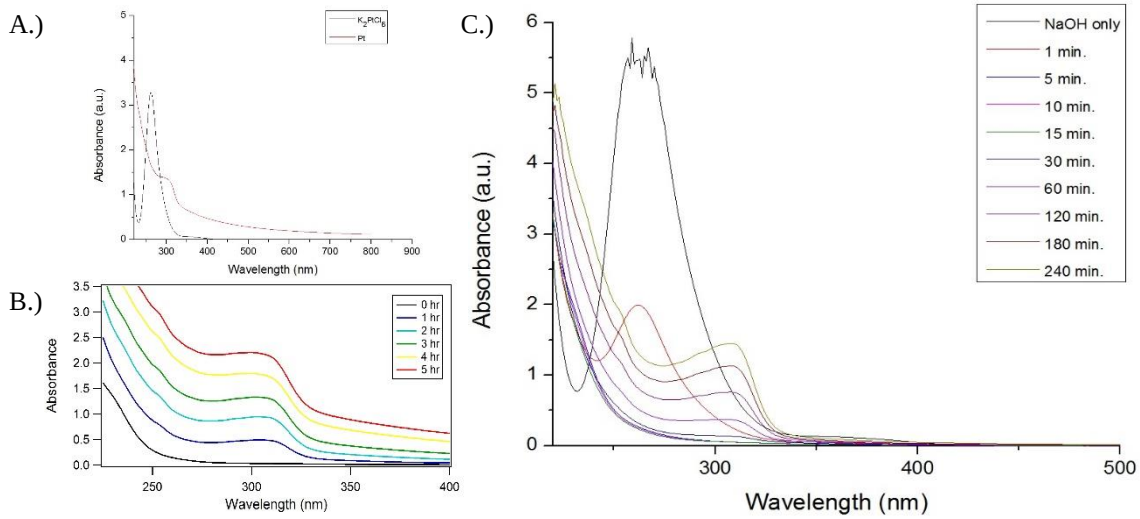

Figure 10. A.) Shown is the UV-Vis spectrum recorded for the K_2PtCl_6 precursor material in aqueous solution and the final Pt product. B.) presents hourly measurements of reaction progress of K_2PtCl_6 in 15mL methanol and 35mL 0.05M NaOH. C.) is a more detailed look at the initial stages of the reaction, from the addition of methanol to the completion of the reaction.

Final Pt solution UV-Vis results typically show a wide absorption band that may mask other chemical species found in the solution, including that of $H_2Pt(OH)_6$. The tailing shown by the final Pt solution in Figure 10a is indicative of colloidal Pt nanoparticles.[62] UV-Vis data taken on a months-old stable Pt sample shows an extended tailing effect to a wavelength of 800nm, while the peak is more broad around 300nm. While no shoulders appear, this is likely due to the fact that the overall Pt curve is masking them. Further research on the intermediate species in the ligand-free Pt synthesis will need to be done using a more sensitive technique, such as ^{195}Pt NMR.

X-ray diffraction of the ligand-free platinum nanoparticles was performed on a powder PANalytical XPert Pro MPD system with a Cu Kα of 0.154 nm. Figure 11b shows the characteristic (111) and (200) peaks for platinum metal at 2θ values of 40° and 46°, respectively, while their corresponding d-spacing values are 0.23nm and 0.20nm.[63]

Following analysis by XRD, images were collected using a Jeol 2010 LaB_6 transmission electron microscope with an accelerating voltage of 200kV. TEM samples were prepared by dissolving a small amount of the sample in 1-2mL of isopropanol (EMD Millipore, DriSolv® anhydrous). Generally, about 25% of the bottom of a 10mL scintillation vial would be covered by the dried nanoparticles before the 1-2mL of isopropanol was added. This was sonicated for 5 minutes before the vial was filled to the top with more isopropanol, producing a very clear-looking dispersion. Samples were then drop-casted into continuous or lacey carbon grids using a glass pipet, covered, and dried overnight. Figure 11c is an analysis of a select group of Pt nanoparticles. The diameter of a sample size of 100 Pt nanoparticles, shown in Figure 11a, was measured using ImageJ. Through this, it was found that the average size of the nanoparticles was 2.5 nm ± 0.5 nm, with the largest nanoparticles reaching 3.5 nm and the smallest occurring at approximately 1.5 nm. Particle size was also measured using a Malvern Zetasizer unit, which indicated that the nanoparticles, while small in size, were agglomerating. On average, the nanoparticle agglomerations were 401.0nm in diameter. Interestingly, the nanoparticles behaved in this way when they were deposited onto carbon TEM grids, as well as $KCa_2Nb_3O_{10}$ supports. Upon observation by TEM, it was found that the Pt nanoparticles formed clusters of >10 when they were deposited onto the support. While they were not aggregating and forming larger nanoparticles, they still tended to form small groups of 1-3nm nanoparticles throughout the sample. Energy dispersive X-ray spectroscopy (EDS) was used to further verify the composition of the nanoparticles to guarantee that the particles were, in fact, platinum.

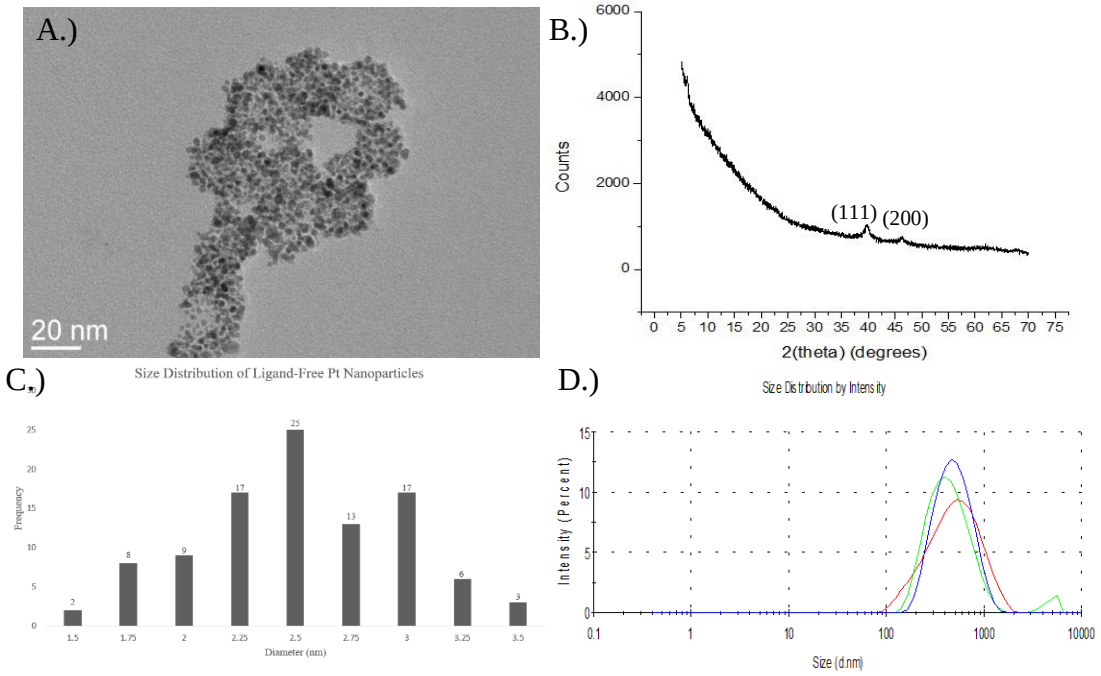

Figure 11. Overview of the resulting Pt nanoparticles from a traditional synthesis. A) presents a sampling of multiply-twinned Pt nanoparticles. B) is the XRD pattern of Pt metal nanoparticles. C) is the size distribution taken from a sample size of 100 Pt nanoparticles from the TEM image shown in A.). D.) is the resulting size distribution of the (presumably agglomerated) Pt nanoparticles in their reaction solution of 0.05M NaOH and methanol.

When heated to temperatures exceeding 900°C in highly reducing conditions, metal oxide nanoparticles commonly undergo agglomeration and sintering. Considering their use as catalysts, their activity is reduced considerably upon exposure to these conditions. Previous work has shown that little to no nanoparticle growth was observed when several types of metal hydroxide nanoparticles were deposited onto $KCa_2Nb_3O_{10}$ and $K_4Nb_6O_{17}$ supports. The results are shown for ligand-free Pt nanoparticles dispersed on re-stacked $KCa_2Nb_3O_{10}$, normally in varying wt. % of 1 up to 5 wt. %. All TEM and high angle annular dark field scanning transmission electron microscopy (HAADF STEM) imaging was performed at 200kV on the Jeol 2010 LaB_6 TEM at the Pennsylvania State University's Materials Characterization Lab (MCL) or on the National Institutes of Standards and Technology (NIST)'s FEI Titan STEM at an accelerating voltage of 300kV. In Figure 12, The Pt nanoparticles decorated the carbon-coated TEM grid with stark uniformity, showing

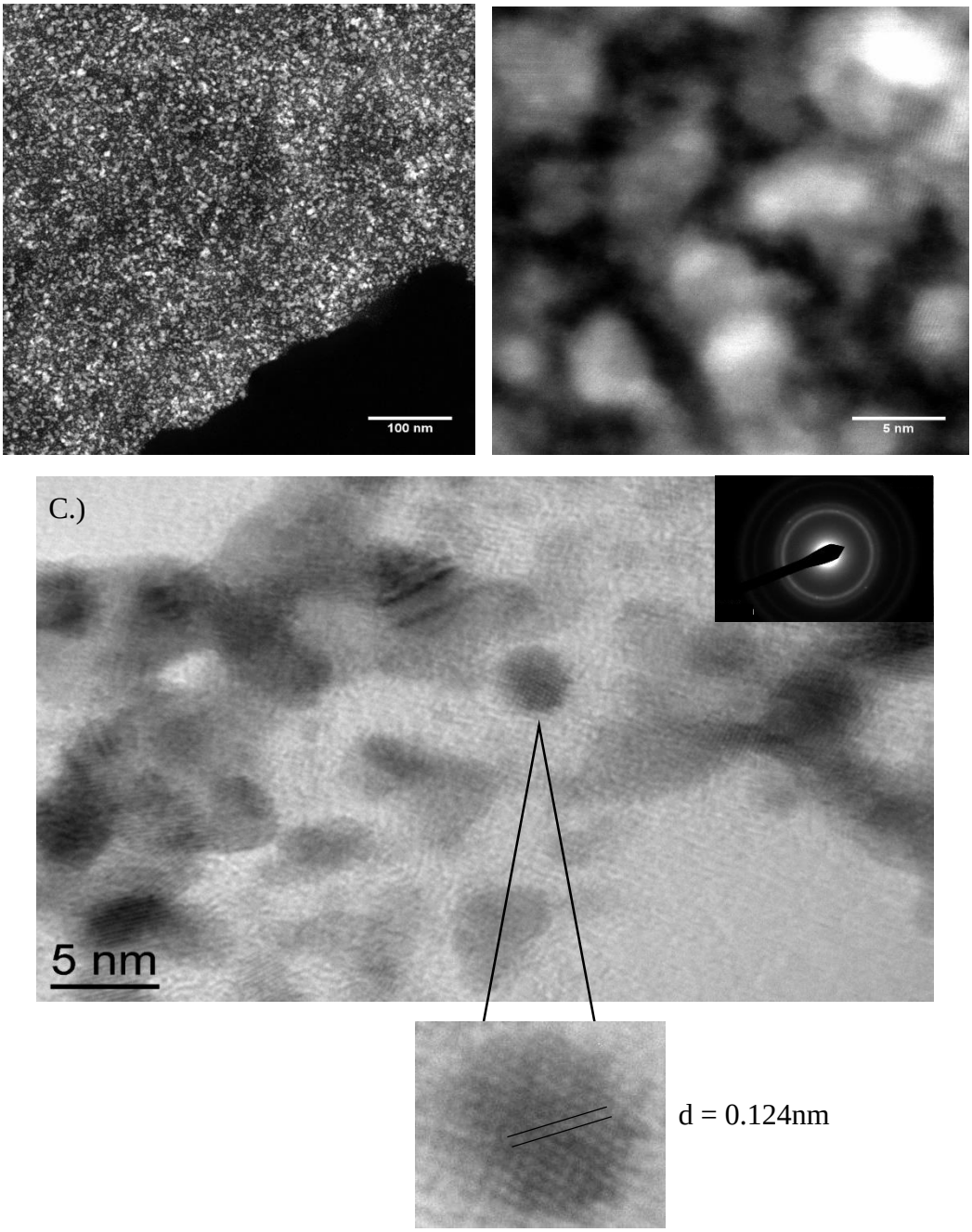

Figure 12. A.) shows a HAADF STEM image examining the extent to which the ligand-free Pt nanoparticles deposited onto the uniform carbon TEM grid. B.), another HAADF STEM image of the same section of carbon TEM grid, presents a closer look at the interactions of the Pt nanoparticles as they were deposited on the grid. C.) TEM results, gathered on a Jeol 2010 LaB_6, of newly-synthesized ligand-free Pt nanoparticles that were deposited and dried directly from solution.

promise as universally available material for use in catalytic materials. Upon closer viewing, it was observed that the nanoparticles were in fact uniformly dispersed and

remained attached to the carbon TEM grid with no response to irradiation by the electron beam. The TEM image in Figure 12c shows clearer detail of the nanoparticles decorating the ultra thin, 4nm-thick carbon grid. Many were shown to be multiply-twinned metal nanoparticles with a d-spacing of approximately 0.124nm, measured in ImageJ. Literature reports the d-spacing of the (111) face at 0.22nm, while indexing of the XRD pattern in Figure 11b shows a d-spacing of 0.23nm.[64]

High angle annular dark field imaging of the behavior of the ligand-free Pt nanoparticles on $KCa_2Nb_3O_{10}$ supports was observed using FEI Titan STEM at the National Institutes of Standards and Technology (NIST) in Gaithersburg, MD. All size distributions are provided using a sample size of 50 nanoparticles per image. Shown below in Figure 13, the Pt nanoparticles appear relatively stable as they are heated from room temperature to 900°C. At 25°C, the Pt nanoparticles on the $KCa_2Nb_3O_{10}$ are relatively

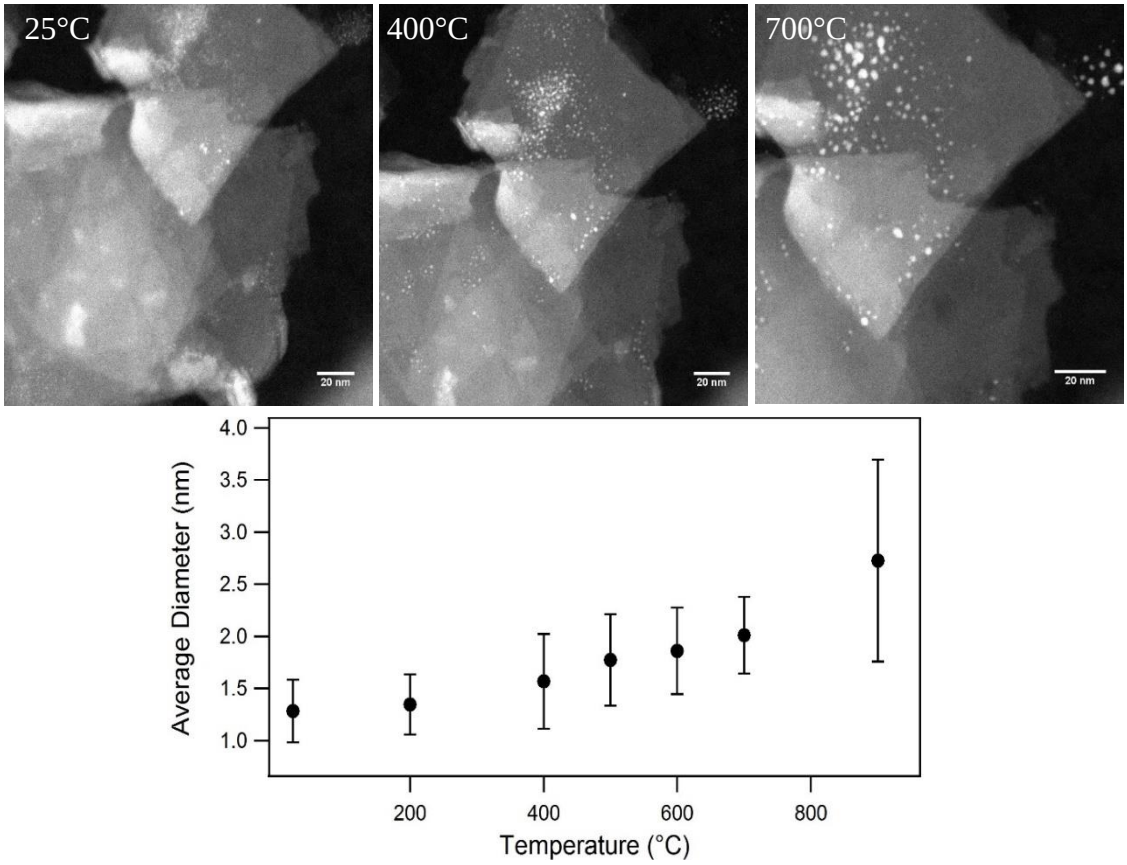

Figure 13. The response of ligand free Pt nanoparticles at room temperature, 400°C, and 700°C. Very limited growth was observed as the temperature was increased at 50°C increments from room temperature. Shown below is the average growth of a sampling of 50 Pt nanoparticles on $KCa_2Nb_3O_{10}$ from the same region at temperatures from 25°C (room temperature) to 900°C.

uniform in size, with a diameter of 1.3nm ±0.3nm. Upon heating to 400°C, the nanoparticles did not undergo large fluctuations in diameter or location; the average size at this temperature remained at 1.6nm ±0.5nm. This slight increase in size can be attributed to some coalescence of Pt nanoparticles, as can be seen in Figure 14. From the 25°C to the 400°C image, the nanoparticles did not increase in size by a full 1nm. At temperatures exceeding 500°C, a small amount of coalescence and growth was seen. In Figure 14 below, coalescence became more prominent as the temperature approached 700°C, which notable instances of this appearing in the top left corner of the image. At the maximum temperature of 900°C, which was chosen because it was the highest temperature at which the $KCa_2Nb_3O_{10}$ nanosheets would not begin to decompose, the size of the Pt nanoparticles was 2.7nm ± 1.0nm. The surprising lack of growth and migration is evidence of strong bonding between the ligand-free Pt nanoparticles and the $KCa_2Nb_3O_{10}$ supports.

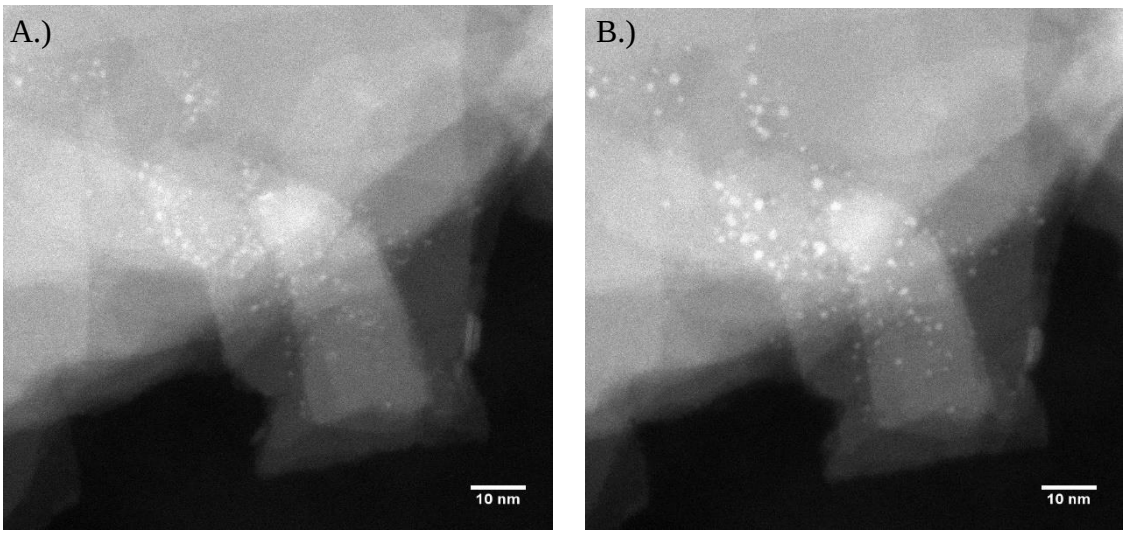

Figure 14. HAADF STEM images taken on the FEI Titan STEM at NIST. A.) presents a select area of ligand-free Pt deposited on a $KCa_2Nb_3O_{10}$ support at room temperature. B.) shows the same area of the grid at 450°C. Here, the nanoparticles have coarsened slightly, with some migration.

The Pt nanoparticles exhibited interesting behavior as they were heated from room temperature to 900°C. Observations of the nanoparticles at 25°C showed them in multiple clusters of ≤10nm that fragmented into smaller, ~1nm nanoparticles once the temperature reached 400°C. However, a very small amount of nanoparticle migration was also observed at this temperature, where it appeared that the Pt nanoparticles were moving together in some places and away from one another in other regions of the grid. This trend continued

as temperatures increased; however, nanoparticle coarsening was not, in fact, a major issue. With an average diameter at 900°C of 2.7nm ± 1.0nm, the size increase from 1.3nm ± 0.3nm at 25°C totals approximately 1nm. Interestingly, the nanoparticles take on a hexagonal appearance at 900°C, which is not as obvious at lower temperatures.

2.5. Zeta Potential of Ligand-free Pt Nanoparticles in Solution.

Zeta potential measurements were done on the ligand-free Pt nanoparticle solution to determine the interaction of the nanoparticle surface with its surrounding reaction solution of 0.05M NaOH and methanol. Because of the difficulty of finding the dielectric constant for a mixture of NaOH and methanol, the nanoparticles were dispersed in a solution of 100% methanol. After 24h, the nanoparticles were still evenly dispersed in the pure methanol, and zeta potential measurements were gathered on the Malvern Zetasizer in DTS 1070 Folded Capillary Zeta Potential Cells. Shown in the zeta potential plot in Figure 15 below, the overall surface charge of the Pt nanoparticles is -10.3mV ± 5.0mV. The negative surface charge on the Pt nanoparticles is likely attributed to adsorbed hydroxide anions on the nanoparticle surface.[47,48,65] As mentioned previously, the negative charge of the hydroxide anion can be transferred to the nanoparticle surface, which increases electrostatic stability of the solution.

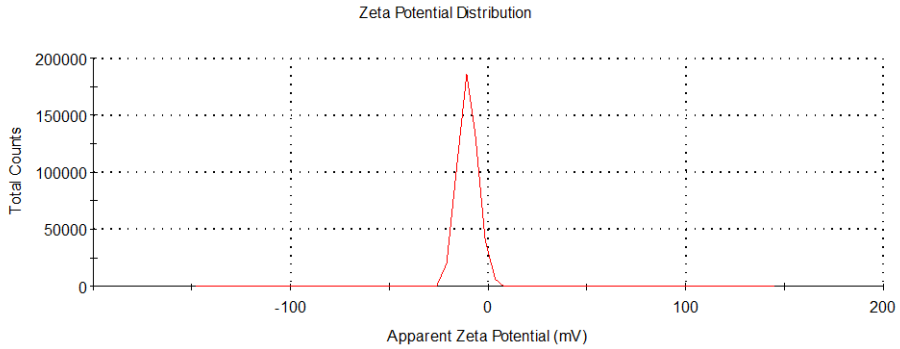

Figure 15. The zeta potential diagram for ligand-free Pt nanoparticles dispersed in methanol.

2.6 Characterization of Ligand-free Pd Nanoparticles

Similar approaches have been taken to synthesize and characterize a stable, ligand-free Pd solution. As before, 0.01 mmol of a palladium metal precursor, K_2PdCl_4, was refluxed at 85°C for 4 hours upon addition of 35mL of 0.05M NaOH and 15mL of DriSolv® methanol. Several attempts at the synthesis showed that the solution changed

color from clear to a dark brown/black after approximately 30 mins.[66] This is a surprising result, considering the Pt synthesis does not experience a rapid color change until after 1 hour of heating at 85°C. These nanoparticles were also unstable in solution, often aggregating the same day they were synthesized and gathering at the bottom of the flask, leaving behind a clear solution. TEM results taken on the Jeol 2010 LaB_6, shown below in Figure 16, present an overview of the Pd nanoparticles produced by the synthesis. The average size of the Pd nanoparticles, taken from a sampling of 100 nanoparticles, is 5.5nm $\pm$ 1.2nm. A prevalence of organic matter was found while viewing many of the Pd nanoparticles samples, which may indicate an excess of methanol. Future work is required for further purification and characterization of these ligand-free Pd nanoparticles, with hope that they will remain stable in solution.

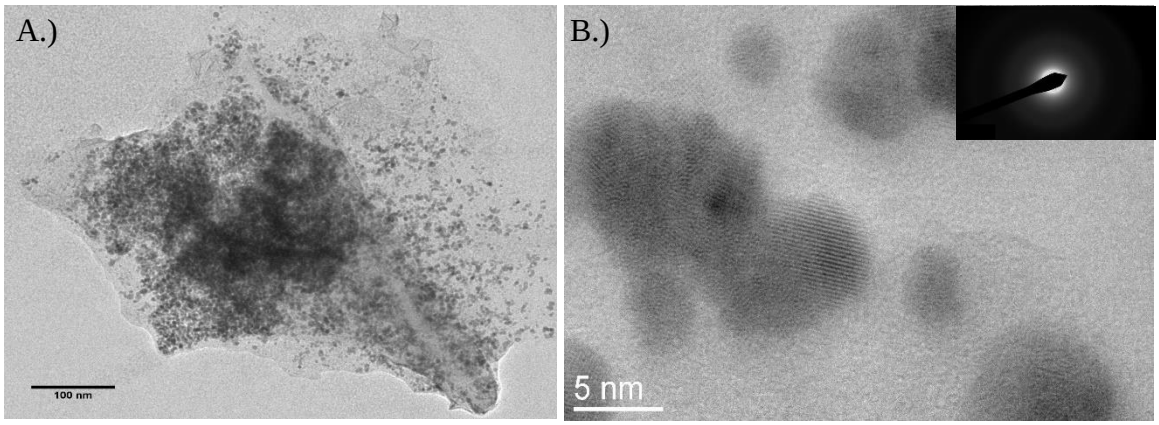

Figure 16. TEM images showing presumed ligand-free Pd nanoparticles. In A.), an overview of commonly found Pd nanoparticle clusters. B.) presents a more defined view of the Pd nanoparticles.

X-Ray diffraction of the Pd nanoparticles revealed much about their composition and their instability in solution. Shown in Figure 17 is the type of XRD pattern produced in the majority of Pd nanoparticle synthesis attempts. The Pd(111) and Pd(200) peaks can be clearly seen at a 2θ of 40° and 46°, respectively.[67,68] The Pd nanoparticle d-spacing for the (111) face is 0.22nm.[68] However, the XRD pattern shows a few additional chemical species they may result from Pd(II) having a much faster ligand exchange rate than Pt(II), which results from its ability to substitute a fifth ligand during the exchange process.[69] For example, PdO is prevalent at 2θ = 34° and 55°, indicating that the Pd is not fully reduced after a reaction time of 72 hours.[70] An interesting addition to the reaction product is Na_2CO_3: the same reactants are used when synthesizing ligand-free Pt and Pd, but Pt XRD

does not indicate the presence of any Na_2CO_3. It may be possible that the Pd in alkaline solution catalyzed a methanol oxidation reaction, thus producing H_2, Na_2CO_3, and CO_2.[71,72] However, this is not seen in the Pt synthesis, so the exact source of the Na_2CO_3 is still unknown.

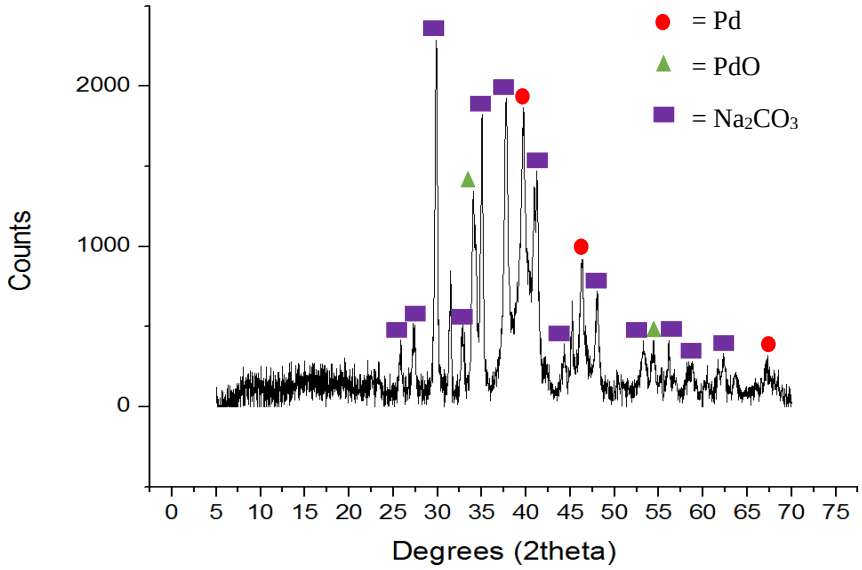

Figure 17. XRD pattern taken of a typical ligand-free Pd synthesis product. It can be seen above that the K_2PdCl_4 precursor was not fully reduced, yet an abundance of unwanted Na_2CO_3 is formed.

CHAPTER 3:
CONCLUSIONS AND FUTURE DIRECTIONS

3.1. Using New Techniques to Investigate Directly the Synthetic Mechanism of Ligand-free Metal Nanoparticles.

The evolution of the ligand-free platinum nanoparticle – from its K_2PtCl_6 precursor to the final, OH^- - stabilized form – can be monitored via ^{195}Pt nuclear magnetic resonance (^{195}Pt NMR) spectroscopy. Earlier studies have utilized ^{195}Pt NMR to investigate the change in Pt-based nanoparticle composition upon acidification of their supporting porous γ-alumina environment.[73] Using this NMR technique, an increase in δ_{Pt} indicates a change from H_2PtCl_6 to $[PtCl_6]^{2-}$. Additionally, but with added difficulty, the species $[PtCl_5(H_2O)]^-$, $[PtCl_5(OH)]^{2-}$, $[PtCl_4(H_2O)_2]$, and $[PtCl_4(OH)_2]^{2-}$ can be detected using ^{195}Pt NMR, while the $[PtCl_4(OH)(H_2O)]^-$ species can be calculated using the relationship between δ_{Pt} and pH of the other Pt compounds.[74] Considering that $\delta_{Pt} = f(pH)$, this relationship may be used to designate approximate δ_{Pt} shifts for unstable aqueous Pt species.

To understand the synthetic mechanism behind the formation of ligand-free metal nanoparticles, ^{195}Pt NMR will prove to be a vital tool. Not only will it detect the proposed hydrolyzed $[MCl_n]^{y-}$ product, it will also indicate which form of $M(OH)_n(H_2O)_y^{x-}$ is most likely to be the dominant species in basic solution. Work from the Didillon group provides a valuable comparison for the Pt-on-metal oxide array, as the group has compiled a list of δ_{Pt} shifts for numerous aqueous Pt species on porous γ-alumina.[73,74] Furthermore, δ_{Pt} from ^{195}Pt NMR can provide additional information regarding the orientation of the aqueous Pt complexes throughout the synthesis to understand possible steric constraints posed by various aqueous Pt complexes. Due to the extremely small (~1 μmol) amount of Pt metal contained in the ligand-free Pt solution, detection of Pt has been arduous, with amounts expected to approach the detection limits of the instrumentation. Scale-up of the ligand-free Pt synthesis produces vastly different results from the original version, presenting new challenges when identifying the synthetic steps in the reaction.

It was noted earlier that small changes in pH during the ligand-free Pt synthesis produced radically different forms of aqueous Pt, with some Pt nanoparticles even being encapsulated in a viscous fluid. The changing reaction pH of the ligand-free Pt solution may also be monitored using ^{195}Pt NMR. Figure 18, shown below, is an example of how

pH changes affect the composition of the aqueous Pt complex. A significant shift in δ_{Pt} from low to high pH could indicate the pH value at which full hydrolysis of the K_2PtCl_6 precursor material is complete, as greater δ_{Pt} are observed with increasing polarity. A sigmoidal curve similar to that in Figure 18 would provide information on the composition and orientation of ligand-free platinum nanoparticles, provided a method of product scale-up can be determined.

3.2. Understanding the Interactions at the Nanoparticle Surface

Aside from understanding the formation mechanism of ligand-free metal

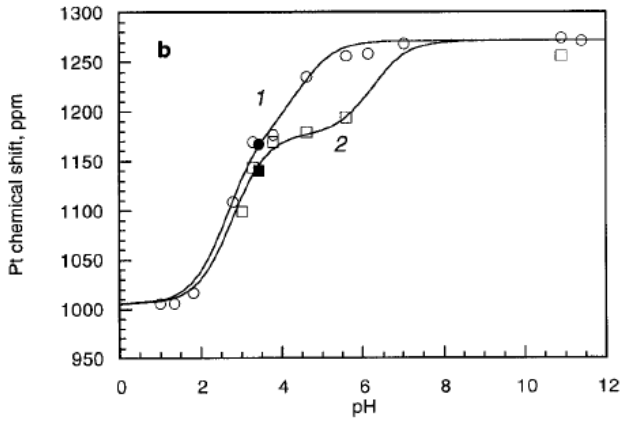

Figure 18. A plot generated from the δ_{Pt} of H_2PtCl_6 in reaction pH values ranging from 0 – 12. The curves are labeled 1 and 2 to correspond with the Pt peak number in Table 2 of the Shelimov et al. paper.[74]

nanoparticles (and all others), investigations into their surface stability will also be underway. If ligand-free versions of metal nanoparticles are to be applied to industrial catalytic reactions, the nanoparticles themselves must first prove their stability in solution. Simple initial tests using zeta potentials garnered from dynamic light scattering (DLS) measurements will indicate the degree of stability of the nanoparticles in solution, as well as the overall surface charging. Current zeta potential readings provide a brief look at the stability of the ligand-free nanoparticles in methanol, but they ultimately do not take the additional stabilization provided by the Na^+ and OH^- ions of the sodium hydroxide in account. Additional zeta potential measurements using electrophoretic light scattering (ELS) methods will be conducted. Here, the nanoparticle's zeta potential can be calculated via the Henry equation using a set of parameters based on the electrokinetics of the nanoparticle in solution:

$$U_E = \frac{2\varepsilon\zeta f(K_a)}{3\eta},$$

where U_E is the electrophoretic mobility, ε is the dielectric constant of the solvent(s), ζ is the zeta potential of the nanoparticles in solution, and η is the solvent viscosity. Henry's function, $f(K_a)$, is often shown as 1.5 in solutions with a moderate to high electrolyte concentration, per the Smoluchowski approximation.[75] However, similar issues arise when using DLS or ELS to determine zeta potential, considering the dielectric constant and viscosity of the solution are still relatively unclear. Determining the dielectric constant for a mixture of sodium hydroxide, water, and methanol will lead to a more accurate representation of the stabilizing effect of the surrounding environment on the ligand-free metal nanoparticle.

As mentioned previously, the concentration of dissolved ions in solution plays a major role in the total stability of the ligand-free nanoparticles in solution with 0.05M NaOH and methanol. In fact, ion concentrations in the mM to μM regime promote nanoparticle stability, while ionic concentrations in greater amounts lead to nanoparticle aggregation.[47] Further work will examine the presumed destabilizing effect of increasing the OH^- concentration of the ligand-free Pt solution. Interestingly, dispersing ligand-free metal nanoparticles in a solution of 0.05M NaOH without methanol has a destabilizing effect on the solution, leading to aggregation. Ligand-free Pt nanoparticles dispersed in DriSolv® methanol did not aggregate and remain dispersed in solution for several days. Varying the concentration of NaOH in which the ligand-free Pt nanoparticles are dispersed and finding their related zeta potentials will provide further details as to why the nanoparticles aggregate under certain ionic concentrations.

It has been reported that ligand-free metal nanoparticles experience vastly different stabilization effects based on the nature of their surrounding ions. For example, chaotropic anions, ions that do little to disrupt the hydrogen bonding in aqueous solutions such as Cl^-, Br^-, and I^-, promote nanoparticle stabilization.[45,46] Kosmotropic anions, those that are strongly attached to water molecules, thus breaking hydrogen bonds, tend to destabilize ligand-free nanoparticles in solutions.[48] These anions are typically those of F^-, SO_4^{2-}, PO_4^{3-}, and so on. Often times, OH^- falls into the kosmotropic regime, meaning it does not provide optimal stability to the nanoparticles in solution.[76] It would be interesting to formulate a solution in which nanoparticle stability is encouraged, perhaps by using a greater concentration of a chaotropic anion such as Cl^- along with the kosmotropic OH^-.

Considering the precursor K_2PtCl_6 solution will release Cl^- anions, it is reasonable to believe that some of the current solution stability arises from the presence of both Cl^- and OH^-. While the concentration of OH^- is currently much higher than that of Cl^-, it may be of interest to monitor the stability of Pt nanoparticles in solution as their concentrations become more equal.

New solution stability problems are introduced when the ligand-free platinum nanoparticles are added to a solution of exfoliated $HCa_2Nb_3O_{10}\cdot 0.5H_2O$. Typically, the $TBA_{0.24}H_{0.76}Ca_2Nb_3O_{10}$ nanosheets are re-stacked using cations such as K^+ or Na^+ after an 18 hour period where the nanoparticles deposit onto the supports. Here, the $TBA_{0.24}H_{0.76}Ca_2Nb_3O_{10}$ nanosheets re-stack instantly upon addition of the ligand-free Pt reaction solution. Presumably, the Na^+ ions remaining from the Pt nanoparticle synthesis are initiating a premature flocculation of the nanosheets, which in turn allows only the smallest ligand-free Pt nanoparticles to become intercalated. An indication of the incomplete nanoparticle deposition is seen in the supernatant fluid left behind, which maintained its dark brown coloration as is characteristic of the ligand-free Pt solution.

Work is being done to change the synthetic method to exclude NaOH. Because the following steps in the nanoparticle deposition require the use of bulky base TBA^+OH^- to break apart the nanosheets, the ligand-free Pt nanoparticle synthesis is currently being done with TBA^+OH^- instead of NaOH. That way, the OH^- is still being provided as surface stabilization for the ligand-free nanoparticles. Figure 19 shows HR-TEM images of

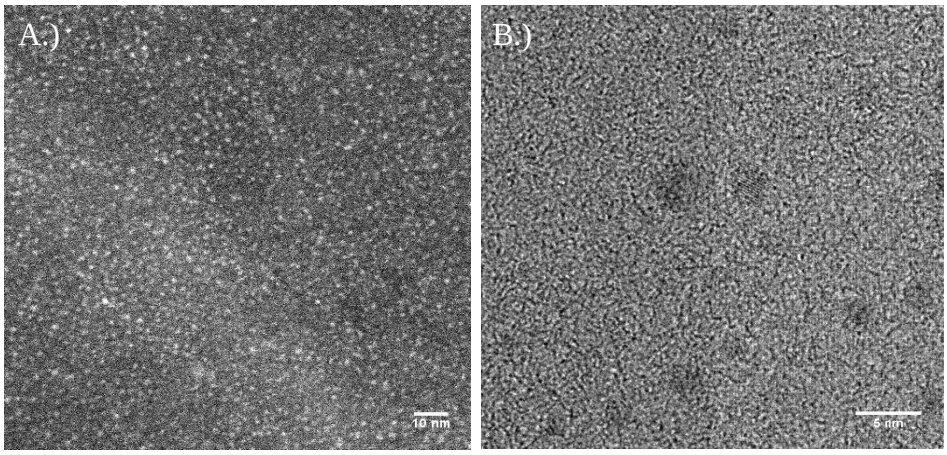

Figure 19. TEM images of possible ligand-free Pt nanoparticles hydrolyzed with the bulky base TBA^+OH^- instead of NaOH. Both are on a carbon support. A.) is a HAADF-STEM image of an assortment of the nanoparticles on the grid. B.) is a TEM image of a select area of the grid and shows the Pt lattice fringes.

proposed ligand-free Pt nanoparticles made with 0.01M TBA^+OH^-. These nanoparticles followed the traditional color changing scheme as those from the NaOH method – clear solution for 2 hours before rapidly changing to yellow/light brown and then to dark brown – but do not maintain the same level of stability, often aggregating over a timespan of days rather than weeks. When the synthesis time was increased to 18 hours, many of the nanoparticles were found deposited on the side of the reaction flask. Additionally, TEM imaging was made difficult by an organic substance, which may have been excess TBA^+OH^-. Further work is being done to improve the TBA^+OH^- synthesis to achieve a stable ligand-free Pt solution.

3.3. Identifying Periodic Trends in Nanoparticle and Support Interactions.

Synthesizing ligand-free metal nanoparticles and understanding their mechanism of formation fits into the overarching theme of designing catalytic systems that maintain their activity for prolonged periods of time. Other facets of the project include investigating the bonding interactions between metal oxide nanoparticles on varying transition metal oxide supports, taking into account these titanate and tungstate supports, among others. In time, ligand-free platinum, palladium, gold, and more will be deposited onto these supports, and trends in the reaction enthalpy will be designed. Because the niobate supports $K_4Nb_bO_{17}$ and $KCa_2Nb_3O_{10}$ have been sufficiently characterized in terms of structure and bonding with metal oxide materials, they will be the supports used for the initial enthalpy of bonding measurements with the ligand-free metal nanoparticles.

Preliminary ITC experiments using ligand-free platinum on $TBA_{0.24}H_{0.76}Ca_2Nb_3O_{10}$ are currently underway on the TA Instruments NanoITC. Showing the necessity of replacing Na^+ with TBA^+ in the nanoparticle synthesis, the ITC power supply could not properly respond to the amount of heat given off by the highly exothermic reaction. This large spike in the power (approximately an order of magnitude higher than in most metal-support systems) needed to maintain isothermal conditions between the two cells of the ITC could possibly be coming from the immense amount of energy released as the Na^+ in solution forces immediate re-stacking of the $TBA_{0.24}H_{0.76}Ca_2Nb_3O_{10}$ sheets. The immediate re-stacking of the $TBA_{0.24}H_{0.76}Ca_2Nb_3O_{10}$ sheets is highly exothermic, which is fitting for the amount of power being supplied to the ITC; however, this masks the bonding enthalpy for ligand-free Pt on $TBA_{0.24}H_{0.76}Ca_2Nb_3O_{10}$. As mentioned above, synthesizing

the ligand-free Pt nanoparticles using 0.01M TBA^+OH^- rather than 0.05M NaOH will eliminate free Na^+ in solution at the time of nanoparticle deposition, lessening the risk of immediate nanosheet flocculation. Additionally, dialyzing away the Na^+ ions will be attempted, if efforts to synthesize TBA^+OH^- - hydrolyzed ligand-free Pt nanoparticles do not produce stable results.

By using the methods described above, a more comprehensive understanding of the formation and stability of these ligand-free metal nanoparticles will be developed. Transmission electron microscopy, both here at Penn State and at NIST, has been a vital tool in monitoring the composition, migration, and growth of the ligand-free Pd and Pt metal nanoparticles. Without X-Ray diffraction techniques, the structures and phase purity of the synthesized niobate, tungstate, and vanadate compounds would still be unknown. UV-Vis spectroscopy was used to approximate the position and timing of structural changes to the Pt nanoparticles, but future work will include analysis by ^{135}Pt NMR to specify the exact intermediates of the synthesis.

Calorimetric methods will be employed to further understand the fundamental chemistry behind catalyst degradation caused by nanoparticle sintering. Gathering information about the strong bonding interactions between ligand-free metal nanoparticles and their niobate supports will provide valuable information regarding their potential to sinter. Once this information has been compared to previous ITC literature regarding metal oxide/hydroxide nanoparticles, work will move to investigate the strong bonding interactions between ligand-free metal nanoparticles and other transition metal oxide supports. These include, but are not limited to, phase pure titanate and tungstate supports. Aside from varying the composition of the ligand-free metal nanoparticle – Pt, Pd, Au, and Ir are currently among those being considered – it may also be necessary to characterize the nanoparticle-support bonding enthalpies based on the size of the deposited nanoparticles. When periodic trends depicting bonding enthalpies of metal nanoparticles on metal oxide supports are further established, use of materials that promote metal nanoparticle sintering on metal oxide support materials will presumably be reduced, and more effective combinations will be used for more effective cleanup and/or catalysis of large-scale productions.

REFERENCES

1. Ferreira, P.J.; la O', G.J.; Shao-Horn, Y.; Morgan, D.; Makharia, R.; Kocha, S.; Gasteiger, H.A. *J. Electrochem. Soc.* **2005,** *152,* A2256-A2271.

2. Hata, H.; Kobayashi, Y.; Bojan, V.; Youngblood, W.J.; Mallouk, T.E. *Nano Lett.* **2008,** *8,* 794-799.

3. Lee, T.; Liu, J.; Chen, N.; Andres, R.P.; Janes, D.B.; Reifenberger, R. *J. Nanopart. Res.* **2000,** *2,* 345-362.

4. Twigg, M.V.; Spencer, M.S. *Appl. Catal. A-Gen.* **2001,** *212,* 161-174.

5. Holby, E.F.; Sheng, W.; Shao-Horn, Y.; Morgan, D. *Energ. Environ. Sci.* **2009,** *2,* 865-871.

6. González-Velasco, J.R.; Botas, J.A.; Ferret, R.; González-Marcos, M.P.; Marc, J.-L.; Gutiérrez-Ortiz, M.A. *Catal. Today* **2000,** *59,* 395-402.

7. Heo, I.; Choung, J.W.; Kim, P.S.; Nam, I.-S.; Song, Y.I.; In, C.B.; Yeo, G.K. *Appl. Catal. B-Environ.* **2009,** *92,* 114-125.

8. Kašpar, J.; Fornasiero, P.; Hickey, N. *Catal. Today* **2003,** *77,* 419-449.

9. Xu, Q.; Kharas, K.C.; Croley, B.J.; Datye, A.K. *ChemCatChem* **2011,** *3,* 1004-1014.

10. Chai, J.; Liao, X.; Giam, L.R.; Mirkin, C.A. *J. Am. Chem. Soc.* **2012,** *134,* 158-161.

11. Shao-Horn, Y.; Sheng, W.C.; Chen, S.; Ferreira, P.J.; Holby, E.F.; Morgan, D. *Top. Catal.* **2007,** *46,* 285-305.

12. Carlton, C.E.; Chen, S.; Ferreira, P.J.; Allard, L.F.; Shao-Horn, Y. *J. Phys. Chem. Lett.* **2012,** *3,* 161-166.

13.Yoshida, K.; Xudong, Z.; Bright, A.N.; Saitoh, K.; Tanaka, N. *Nanotechnology* **2013,** *24,* 065705.

14. Tauster, S.J.; Fung, S.C.; Baker, R.T.K.; Horsley, J.A. *Science* **1981,** *211,* 1121-1125.

15. Belton, D.N.; Sun, Y.-M.; White, J.M. *J. Am. Chem. Soc.* **1984,** *106,* 3060-3062.

16. Fu, Q.; Wagner, T.; Olliges, S.; Carstanjen, H.-D. *J. Phys. Chem. B* **2005,** *109,* 944-951.

17. Liu, G.F.; Sroubek, Z.; Yarmoff, J.A. *Phys. Rev. Lett.* **2004,** *92,* 216801-1 – 216801-4.

18. Liu, X.; Liu, M.-H.; Luo, Y.-C.; Mou, C.-Y.; Lin, S.D.; Cheng, H.; Chen, J.-M.; Lee, J.-F.; Lin, T.-S. *J. Am. Chem. Soc.* **2012,** *134,* 10251-10258.

19. Wang, J.; Lu, A.-H.; Li, M.; Zhang, W.; Chen, Y.-C.; Tian, D.-X.; Li, W.-C. *ACS Nano* **2013,** *7,* 4902-4910.

20. Dai, Y.; Lim, B.; Yang, Y.; Cobley, C.M.; Li, W.; Cho, E. C.; Grayson, B.; Fanson, P.T.; Campbell, C.T.; Sun, Y.; Xia, Y. *Angew. Chem. Int. Edit.* **2010,** *49,* 8165-8168.

21. Campbell, C.T.; *Nat. Chem.* **2012,** *4,* 597-598.

22. Rodriguez, J.A.; Liu, P.; Hrbek, J.; Evans, J.; Pérez, M. *Angew. Chem. Int. Edit.* **2007,** *46,* 1329-1332.

23. Farmer, J.A.; Campbell, C.A. *Science* **2010,** *329,* 933-936.

24. Schwartz, J.M.; Schmidt, L.D. *J. Catal.* **1992,** *138,* 283-293.

25. Kundakovic, L.; Flytzani-Stephanopoulos, M. *J. Catal.* **1998,** *179,* 203-221.

26. Jarvis, E.; Carter, E. *Phys. Rev. B* **2002,** *66,* 100103-1 – 100103-4.

27. Strayer, M.E.; Binz, J.M.; Tanase, M.; Sharma, R.; Rioux, R. M.; Mallouk, T.E. *J. Am. Chem. Soc.* **2014,** *136,* 5687–5696.

28. Brewer, L.; *Acta Metall. Mater.* **1967,** *15,* 553-556.

29. Ma, R.; Kobayashi, Y.; Youngblood, W.J.; Mallouk, T.E. *J. Chem. Mater.* **2008,** *18,* 5982-5985.

30. Karp, E.M.; Silbaugh, T.L.; Campbell, C.T. *J. Am. Chem. Soc.* **2013,** *135,* 5208-5211.

31. Kong, D.; Wang, G.; Pan, Y.; Hu, S.; Hou, J.; Pan, H.; Campbell, C.T.; Zhu, J. *J. Phys. Chem. C* **2011,** *115,* 6715-6725.

32. Freyer, M.W.; Lewis, E.A. *Method Cell Biol.* **2008,** *84,* 79-112.

33. Lew, W.; Crowe, M.C.; Karp, E.; Lytken, O.; Farmer, J.A.; Árnadóttir, L.; Schoenbaum, C.; Campbell, C.T. *J. Phys. Chem., C* **2011,** *115,* 11586-11594.

34. Lew, W.; Crowe, M.C.; Campbell, C.T.; Carrasco, J.; Michaelides, A. *J. Phys. Chem., C* **2011,** *115,* 23008-23012.

35. Hodgson, A.; Haq, S. *Surf. Sci. Rep.* **2009,** *64,* 381-451.

36. Campbell, C.T. *Accounts Chem. Res.* **2013,** *46,* 1712-1719.

37. Dion, M.; Ganne, M.; Tournoux, M. *Mat. Res. Bull.* **1981,** *16,* 1429-1435.

38. Maeda, K.; Eguchi, M.; Lee, S.-H.; Youngblood, J.; Hata, H.; Mallouk, T.E. *J. Phys. Chem., C* **2009,** *113,* 7962-7969.

39. Ebina, Y.; Sasaki, T.; Harada, M.; Watanabe, M. *Chem. Mater.* **2002,** *14,* 4390-4395.

40. Schaak, R.E.; Mallouk, T.E. *Chem. Commun.* **2002,** 706-707.

41. Behafarid, F.; Cuenya, B.R. *Surf. Sci.* **2012,** *606,* 908-918.

42. Choudhary, V.R.; Mondal, K.C.; Mamman, A.S. *J. Catal.* **2005,** *233,* 36-40.

43. Petkovic, L.M.; Ginosar, D.M.; Rollins, H.W.; Burch, K.C.; Pinhero, P.J.; Farrell, H.H. *Appl. Catal., A* **2008,** *338,* 27-36.

44. Ertl, G.; Knozinger, H.; Weitkamp, J. *The Handbook of Heterogeneous Catalysis*; Wiley-VCH: Weinhein, Germany, 1997.

45. Sylvestre, J.P.; Poulin, S.; Kabashin, A.V.; Sacher, E.; Meunier, M.; Luong, J.H.T. *J. Phys. Chem., B* **2004,** *108,* 16864-16869.

46. Šišková, K.; Vlčková, B.; Turpin, P.Y.; Fayet, C.; *J. Phys. Chem., C* **2008,** *112,* 4435-4443.

47. Merk, V.; Rehbock, C.; Becker, F.; Hagemann, U.; Nienhaus, H.; Barcikowski, S. *Langmuir* **2014,** *30,* 4213-4222.

48. Pfeiffer, C.; Rehbock, C.; Hühn, D.; Carrillo-Carrion, C.; Jimenez de Aberasturi, D.; Merk, V.; Barcikowski, S.; Parak, W.J. *J. R. Soc. Interface* **2014,** *11,* 20130931.

49. Rehbock, C.; Merk, V.; Gamrad, L.; Streubel, R.; Barcikowski, S. *Phys. Chem. Chem. Phys.* **2013,** *15,* 3057-3067.

50. Bae, C.H.; Nam, S.H.; Park, S.M. *Appl. Surf. Sci.* **2002,** *197,* 628-634.

51. Herricks, T.; Chen, J.; Xia, Y. *Nano Lett.* **2004,** *4,* 2367-2371.

52. Sasaki, T.; Komatsu, Y.; Fujiki, Y. *Chem. Mater.* **1992,** *4,* 894-899.

53. Sasaki, T.; Watanabe, M.; Michiue, Y.; Komatsu, Y.; Izumi, F.; Takenouchi, S. *Chem. Mater.* **1995,** *7,* 1001-1007.

54. Grey, I.E.; Li, C.; Madsen, I.C.; Watts, J.A. *J. Solid State Chem.* **1987,** *66,* 7-19.

55. Grey, I.E.; Madsen, I.C.; Watts, J.A. *J. Solid State Chem.* **1985,** *58,* 350-356.

56. Kudo, A.; Omori, K.; Kato, H. *J. Am. Chem. Soc.* **1999,** *121,* 11459-11467.

57. Evans, H.T.; Brusewitz, A.M. *Acta Chem. Scand.* **1994,** *48,* 533-536.

58. Hawthorne, F.C.; Calvo, C. *J. Solid State Chem.* **1977,** *22,* 157-170.

59. *Chemical Information Review Document for Oral Exposure to Tetravalent and Pentavalent Vanadium Compounds*; U.S. Department of Health and Human Services; 2008; 10-11.

60. Briskeby, S.T.; Tsypkin, M.; Tunold, R.; Sunde, S. *RSC Adv.* **2014,** *4,* 44185-44192.

61. Huang, C.-H.; Wang, I.-K.; Lin, Y.-M.; Tseng, Y.-H.; Lu, C.-M. *J. Mol. Catal. A: Chem.* **2010,** *316,* 163-170.

62. Creighton, J.A.; Eadon, D.G.; *J. Chem. Soc. Faraday Trans.* **1991,** *87,* 3881-3891.

63. Shao, Z.-G.; Zhu, F.; Lin, W.-F.; Christensen, P.A.; Zhang, H. *Phys. Chem. Chem. Phys.* **2006,** *8,* 2720-2726.

64. Zhang, B.; Wang, D.; Hou, Y.; Yang, S.; Yang, X. H.; Zhong, J.H.; Liu, J.; Wang, H.F.; Hu, P.; Zhao, H.J.; Yang, H.G. *Sci. Rep.* **2013,** *3,* 1836.

65. Verwey, E.J.W; de Boer, J.H. *Recl. Trav. Chim. Pay-B* **1936,** *55,* 675-687.

66. Kim, S.-W.; Park, J.; Jang, Y.; Chung, Y.; Hwang, S.; Hyeon, T. *Nano Lett.* **2003,** *3,* 1289-1291.

67. Lu, L.; Wang, H.; Xi, S.; Zhang, H. *J. Mater. Chem.* **2002,** *12,* 156-158.

68. Navaladian, S.; Viswanathan, B.; Varadarajan, T.K.; Viswanath, R.P. *Nanoscale Res. Lett.* **2009,** *4,* 181-186.

69. Langford, C.H.; Gray, H.B. *Ligand Substitution Processes,* 1st ed.; W.A. Benjamin, Inc.: New York, 1966; pp 45-50.

70. Baylet, A.; Marécot, P.; Duprez, D.; Castellazzi, P.; Groppi, G.; Forzatti, P. *Phys. Chem. Chem. Phys.* **2011,** *13,* 4607-4613.

71. Pandey, R.K.; Lakshminarayanan, V. *J. Phys. Chem., C* **2009,** *113,* 21596-21603.

72. Onwudili, J.A.; Williams, P.T. *Green Chem.* **2010,** *12,* 2214-2224.

73. Shelimov, B.; Lambert, J.-F.; Che, M.; Didillon, B. *J. Catal.* **1999**, *185,* 462-478.

74. Shelimov, B.; Lambert, J.-F.; Che, M.; Didillon, B. *J. Am. Chem. Soc.* **1999,** *121*, 545-556.

75. Kaszuba, M.; Corbett, J.; Watson, F.M.; Jones, A. *Phil. Trans. R. Soc.* **2010,** *368,* 4439-4451.

76. Lynden-Bell, R.M.; Morris, S.C.; Barrow, J.D.; Finney, J.L.; Harper, C. *Water and Life: The Unique Properties of H_2O,* 1st ed.; CRC Press, 2010; pp 79-80.